3D translational landslide evolution in sensitive soils

Wangcheng Zhang[1] and Alexander M. Puzrin[1]

[1]ETH Zurich

November 22, 2022

Abstract

Translational landslides in sensitive soils are usually enormous in size but often developed from a minute slip surface. Attention has previously been paid to quantifying the failure initiation of a translational landslide through two-dimensional (2D) plane strain slope stability analyses. The findings of failure initiation from the 2D simplifications need to be justified in a realistic 3D scenario, and more importantly, are inconvenient to apply into analysing the subsequent 3D post-failure behaviours. This study aims to explore 3D translational landslide evolution integrating both the failure initiation and post-failure behaviours by using an original Lagrangian-Eulerian depth-integrated finite volume scheme. The numerical method is formulated by solving governing equations in terms of the conservations of mass and momentum considering isotropic and linear strain softening materials. Ability of this framework to simulate a complete 3D landslide evolution, including the initiation and growth of slip surface, global slab failure, post-failure behaviours and re-deposition, has been demonstrated for different 3D slope geometries. The proposed numerical scheme is able to capture diverse post-failure behaviours, such as retrogression and blocky slide mass, in sensitive soils. The characteristics of the slip surface growth within a favoured layer and the patterns of the global slab failure in the overlying layer have been thoroughly discussed. For planar slopes, it helps to establish an analytical criterion for unstable dynamic growth of a planar slip surface, which can optimise the slope stability analysis in sensitive soils.

3D TRANSLATIONAL LANDSLIDE EVOLUTION IN SENSITIVE SOILS

Manuscript submitted to Journal of Geophysical Research: Earth Surface on 18/11/2021

Wangcheng Zhang
Postdoctoral Fellow
Institute for Geotechnical Engineering, ETH Zurich
Stefano Franscini Platz 5, 8093 Zurich, Switzerland
Email: wangcheng.zhang@igt.baug.ethz.ch

Alexander M. Puzrin
Professor
Institute for Geotechnical Engineering, ETH Zurich
Stefano Franscini Platz 5, 8093 Zurich, Switzerland
Email: alexander.puzrin@igt.baug.ethz.ch

No of words (excluding abstract, acknowledgements and references): 8869
No of figures: 21
No of tables: 3

3D translational landslide evolution in sensitive soils

ABSTRACT

Translational landslides in sensitive soils are usually enormous in size but often developed from a minute slip surface. Attention has previously been paid to quantifying the failure initiation of a translational landslide through two-dimensional (2D) plane strain slope stability analyses. The findings of failure initiation from the 2D simplifications need to be justified in a realistic 3D scenario, and more importantly, are inconvenient to apply into analysing the subsequent 3D post-failure behaviours. This study aims to explore 3D translational landslide evolution integrating both the failure initiation and post-failure behaviours by using an original Lagrangian-Eulerian depth-integrated finite volume scheme. The numerical method is formulated by solving governing equations in terms of the conservations of mass and momentum considering isotropic and linear strain softening materials. Ability of this framework to simulate a complete 3D landslide evolution, including the initiation and growth of slip surface, global slab failure, post-failure behaviours and re-deposition, has been demonstrated for different 3D slope geometries. The proposed numerical scheme is able to capture diverse post-failure behaviours, such as retrogression and blocky slide mass, in sensitive soils. The characteristics of the slip surface growth within a favoured layer and the patterns of the global slab failure in the overlying layer have been thoroughly discussed. For planar slopes, it helps to establish an analytical criterion for unstable dynamic growth of a planar slip surface, which can optimise the slope stability analysis in sensitive soils.

Keywords: translational landslides, sensitive soil, landslide evolution, slip surface growth, 3D slope geometry

PLAIN LANGUAGE SUMMARY

Translational landslides in sensitive soils are often huge and catastrophic with considerable failure extension from a minute initiation region. Our knowledge of why and how the progressive failure in translational landslides evolves is limited but it likely results from slip surface growth within a favored weak layer. The mechanisms causing the underneath slip surface growth and the whole evolution of translational landslides are difficult to assess at the landscape scale even with the aids of state-of-the-art geophysical and geological investigations. Advanced numerical modelling is an alternative approach to improve our understanding towards the three-dimensional (3D) evolution of translational landslides. Here, we propose such an original numerical method formulated from the fundamental laws of thermodynamics and soil plasticity theory. We simulated the dynamic slip surface growth from a small pre-failure zone within the weak layer and improved the assessment of its critical size for the catastrophic slip surface growth. Our criterion shows, upon critical conditions, a slip surface can grow and become as large as ~100 km^2 within minutes. This is followed by global slab failure in the overlying layer with retrogression upslope and ploughing downslope. Simulated post-failure behaviours with true 3D slope geometries are slightly affected by the horizontal slope gradient but significantly depend on the vertical slope gradient. Our findings improve understanding of how an insignificant pre-failure zone rapidly grows into an enormous slip surface and eventually evolves into a translational landslide with progressive failure in sensitive soils.

INTRODUCTION

Slope stability analysis and assessment of landslide dynamics are important areas of study for engineering geology professionals and geotechnical engineers. In practice, they are usually simplified as two-dimensional (2D) plane strain problems (e.g., Morgenstern and Price 1965, Spencer 1967, Cornforth 2005), which have been considered conservative in the Limit Equilibrium Method (LEM), as resistances from the out-of-plane direction are ignored. However, the 2D simplification needs the justification that the linear cross section chosen from a three-dimensional (3D) ground is the most 'pessimistic' (Duncan 1996). This is not an easy task in realistic complex terrain, where the most pessimistic section, if it can be found, is most likely nonlinear. To partly avoid such a geometrical uncertainty, slope stability analysis might, in practice, be conducted for multiple cross sections of a single slope, which could be a huge workload for risk assessment and mapping of a large area involved in an engineering project such as the determination of a subsea pipeline route.

Moreover, for slope failure in sensitive soils, shearing failure within a basal slip surface might lead to the growth of the slip surface, eventually evolving into a translational landslide such as the well-known enormous Storegga Slide offshore Norway (Kvalstad et al. 2005, Micallef et al. 2007) or the massive retrogressive landslide in December 2020 at Gjerdrum, Norway, which caused seven deaths. The slip surface of translational landslides can grow in any direction within a favoured 'weak' layer, which may or may not be parallel to the main travel direction of the slide mass (Zhang et al. 2020). Such a multi-directional propagation mechanism can provide additional driving force because of the reduction in strength during slip surface growth, but this cannot be considered in a 2D case. Hence, the 2D simplification with assumed travel direction might be nonconservative for the assessment of the progressive failure of translational landslides in sensitive soils.

Because of greater computational capacity, studies have been able to consider 3D slope stability analysis in the last several decades (Hungr et al. 1989, Lam and Fredlund 1993, Huang and Tsai 2000, Cheng and Yip 2007), although most of them have focused on rotational slide mechanisms using the LEMs. Some more sophisticated 3D models for slope stability problems have been emerging that use numerical methods such as the Finite Element Method (Griffiths and Marquez 2007, Lin et al. 2020) and Finite Difference Method (Zhang et al. 2013).

The LEM and most existing numerical methods reach their limits in carrying out satisfactory stability analyses of slopes with sensitive clays against potential translational landslides, due to the progressive failure process and large deformation involved (Puzrin et al. 2004, 2016, Locat et al. 2011, Zhang et al. 2015). Instead, some recent studies have explored simplified analytical criteria for 3D translational landslide initiation in sensitive clays by interpretation and quantification of slip surface growth along a weak layer (Zhang et al. 2020, Klein and Puzrin 2021), based on planar or idealised conical geometry and static conditions. The applicability of these criteria to realistic dynamic conditions and complex geometry remains uncertain. Meanwhile, the transition from growth of slip surface to global failure in 3D situations is still an open issue.

Another important issue in assessing the risk of slope instability is the modelling of landslide dynamics and its evolution, which can be performed by using large deformation numerical methods such as the depth-integrated method (Hungr 1995, Liu and Huang 2006, Zhang and Puzrin 2021), computational fluid dynamics (Biscarini 2010), smoothed particle hydrodynamics (Zhang et al. 2020) or the material point method (Dong et al. 2017). However, most of these are 2D in nature and need the input of details of the initial slide mass such as geometry, volume and initial velocity, which are rarely determined in practice. A correlation between slope stability analysis (landslide initiation) and evolved debris flow (landslide dynamics) in 3D is required for fully understanding 3D landslide evolution and hence for optimised risk assessment.

In this study, the whole evolution of 3D translational landslides in sensitive soils, covering the failure initiation, slip surface growth, slab failure and post-failure behaviours, is observed and discussed through an original Lagrangian-Eulerian depth integrated numerical analysis. The governing equations of the problem are formulated based on conservation of mass and momentum. The solutions of landslide dynamics are obtained from a finite volume scheme with a staggered mesh strategy. New criteria for slip surface growth in planar slopes are proposed and quantifications of slab failure are discussed based on the numerical investigations, which are expected to facilitate slope stability analysis and risk assessment of landslides in sensitive clays. Finally, ability of the framework to account for the effects of the true 3D slope geometry has been demonstrated.

3D NUMERICAL SCHEME FOR MODELLING LANDSLIDE EVOLUTION IN SENSITIVE CLAYS

Problem description

Translational or spread landslides are common in northern countries, such as Norway and Canada, and offshore continental slopes where sensitive clays are abundant (Skempton 1985, L'Heureux et al. 2012, Issler et al. 2015). Figure 1 shows a conceptual evolution of typical submarine landslides. Although their scales are usually very large (for example, the Storegga Slide covered between 2500 and 3500 km^2 of sediment (Haflidason et al. 2004)), translational slides might be initiated at a minute slip surface, as shown in Figure 1a, triggered by external factors such as earthquakes. An initial slip surface is often concentrated in a favoured soil layer (the so-called 'weak layer') where shear strength relative to the overburden pressure is lower than adjacent layers. The weak layer provides a locus for progressive growth of the slip surface with extensive external triggers, as shown in Figure 1b. Once the size of the slip surface reaches a threshold, the slip surface growth becomes catastrophic and can only be limited by slope flattening or global slab failure, as shown in Figure 1c. Diverse post-failure behaviours, such as retrogression upslope and progressive ploughing or debris flow downslope, may present after the global slab failure (Zhang et al. 2021), as shown in Figure 1d.

Governing equations

In order to analyse slope stability and evolution of landslides in sensitive soils, the domain of interest is essentially divided into regularised cells, with each cell holding characteristics of the evolving landslide, as shown in Figure 2. Note that the bathymetry map, showing a submarine landslide offshore Scotland (after Carter et al. 2020) is just for illustration. The edges of the cell are parallel to the axes of coordinates x and y, and the x–y plane ($z = 0$) was set as the horizontal plane and crossing through a reference point (taken as the slope centre in the study) at the basal slip surface. Cells are fixed during the landslide process, with materials travelling through them, forming an Eulerian framework. Conservations of mass and momentum are then formulated within each cell, and global instability can be modelled by integrating all cells with consideration of proper inter-cell constitutive models and fluxes.

Key assumptions for establishing governing equations are as follows.

- The thickness of the landslide is small (<1:10) compared to its dimensions, so that the velocity can be averaged along the depth of each cell.
- Momentum of the slide mass along the z-direction is negligible.
- Trapped water moves together with soils in each cell, and any generated pore pressures have no time to dissipate, ensuring an undrained (and incompressible) condition.

Based on these assumptions, conservation of mass in each cell can be expressed by

$$\frac{\partial h}{\partial t} + \frac{\partial hu}{\partial x} + \frac{\partial hv}{\partial y} = 0 \tag{1}$$

where h is the height of the cell, u and v are the velocity in the x- and y-directions (as shown in Figure 2), respectively, and t is the elapsed time. Conservation of momentum in each cell is given by

$$\frac{\partial hu}{\partial t}+\frac{\partial hu^2}{\partial x}+\frac{\partial h\sigma_x}{\rho\partial x}+\frac{\partial huv}{\partial y}-\frac{\partial h\tau_{xy}}{\rho\partial y}-\frac{\tau_{w,x}+\tau_{g,x}+\tau_{drag,x}}{\rho}=0 \tag{2}$$

and

$$\frac{\partial hv}{\partial t}+\frac{\partial hv^2}{\partial y}+\frac{\partial h\sigma_y}{\rho\partial y}+\frac{\partial huv}{\partial x}-\frac{\partial h\tau_{xy}}{\rho\partial x}-\frac{\tau_{w,y}+\tau_{g,y}+\tau_{drag,y}}{\rho}=0 \tag{3}$$

for the x- and y-directions, respectively. In the above equations, σ_x, σ_y and τ_{xy} are stress components applied at the centre of the cell face, with the face normals parallel to the x or y axis; $\tau_{\mathrm{w},x}$ and $\tau_{\mathrm{w},y}$ are weak layer (or slip surface) shear stress components; $\tau_{\mathrm{g},x}$ and $\tau_{\mathrm{g},y}$ are gravity shear stress components at the buried depth of the weak layer; and $\tau_{\mathrm{drag},x}$ and $\tau_{\mathrm{drag},y}$ are drag shear stress components.

Stress components at cell face centre

Usually, the stress tensor ($\boldsymbol{\sigma}$) describing the stress status at the centre of the cell face can be decomposed into

$$\boldsymbol{\sigma}=\boldsymbol{s}+p\cdot\boldsymbol{I} \tag{4}$$

where $\boldsymbol{s}$ is the deviatoric stress tensor, p the mean stress and $\boldsymbol{I}$ the second-order identity tensor. Note that the vertical normal stress component σ_z can be expressed by

$$\sigma_z=\frac{1}{2}\gamma' h \tag{5}$$

where γ' is the submerged unit weight of soils.

Similarly, the strain tensor ($\boldsymbol{\varepsilon}$) can be decomposed into

$$\boldsymbol{\varepsilon}=\boldsymbol{e}+\frac{\varepsilon_v}{3}\cdot\boldsymbol{I} \tag{6}$$

where $\boldsymbol{e}$ is the deviatoric strain tensor and ε_{v} the volumetric strain. It can also be divided into the elastic and plastic portions, which will be denoted by superscripts 'e' and 'p', respectively, in the remainder of the paper. Note that the volumetric strain satisfies $\varepsilon_{\mathrm{v}} = \varepsilon_{\mathrm{v}}^{\mathrm{e}} = \varepsilon_{\mathrm{v}}^{\mathrm{p}} \to 0$, as the undrained condition was maintained and the von Mises yield criterion with an associated flow rule was used. Hence, one may write $\boldsymbol{\varepsilon} \cong \boldsymbol{e}$, $\boldsymbol{\varepsilon}^{\mathrm{e}} \cong \boldsymbol{e}^{\mathrm{e}}$, and $\boldsymbol{\varepsilon}^{\mathrm{p}} \cong \boldsymbol{e}^{\mathrm{p}}$. The elasticity of materials is assumed linear and isotropic, and therefore the deviatoric stress tensor is expressed by

$$\boldsymbol{s} = 2G\boldsymbol{e}^{e} \cong 2G\boldsymbol{\varepsilon}^{e} \tag{7}$$

where G is the shear modulus.

A modified von Mises yield criterion was adopted in order to consider isotropic and linear strain softening, given by

$$q = max\left(1 - \frac{\varepsilon_s^p}{\varepsilon_{s,r}^p},\ \ \frac{1}{S_t}\right) \cdot 2s_{us,p} \tag{8}$$

where $q = \sqrt{\frac{3}{2}}\|\boldsymbol{s}\|$ is the deviatoric stress, $s_{\mathrm{us,p}}$ the peak undrained shear strength in the sliding layer which can be measured from a triaxial element test; $\varepsilon_{\mathrm{s}}^{\mathrm{p}} = \int_0^t \sqrt{\frac{2}{3}}\|\dot{\boldsymbol{e}}^{\mathrm{p}}\|dt$ the accumulated plastic deviatoric strain; $\varepsilon_{\mathrm{s,r}}^{\mathrm{p}}$ the accumulated deviatoric strain to the residual shear strength; S_{t} the soil sensitivity defining the ratio of the peak and residual shear strengths. $\varepsilon_{\mathrm{s,r}}^{\mathrm{p}}$ can be determined from a triaxial test by $\varepsilon_{\mathrm{s,r}}^{\mathrm{p}} = \frac{2}{3}\gamma_{\mathrm{r}}^{\mathrm{p}}$ where $\gamma_{\mathrm{r}}^{\mathrm{p}}$ is the plastic shear strain associated to the residual undrained shear strength.

The softening and associated flow rules used for calculating stress components on the cell faces are also depicted in Figure 3a. The solid circle represents the current yield surface in the meridian plane while the dashed circle represents the softening yield surface. With an incremental deviatoric strain tensor, soils may move from the initial elastic state *A* to the plastic state *B* (see Figure 3a). An intermediate virtual state *T* outside the yield surfaces was assumed, in order to calculate the plastic strain. According to equations (7) and (8), one may write

$$\boldsymbol{OA} = 2G\boldsymbol{e}^{e,A}; \boldsymbol{OB} = 2G\boldsymbol{e}^{e,B}; \boldsymbol{AT} = 2G\Delta\boldsymbol{e}; \boldsymbol{BT} = 2G\Delta\boldsymbol{e}^{p}; \boldsymbol{BT}' = \frac{4}{3}\frac{s_{us,p}}{\varepsilon_{s,r}^{p}}\Delta\boldsymbol{e}^{p} \tag{9}$$

where T' is the intersect of the line BT and the current yield surface. As the radius of the current yield surface (the solid circle) is $R_{\mathrm{ys}} = \sqrt{\frac{2}{3}}d\left(\varepsilon_{\mathrm{s}}^{\mathrm{p}}\right)$, the incremental plastic deviatoric strain can then be calculated based on the geometric relationship, by

$$\begin{aligned} R_{ys} - \|\boldsymbol{BT}'\| = \|\boldsymbol{OT}\| - \|\boldsymbol{BT}\| \rightarrow \sqrt{\frac{2}{3}}d\left(\varepsilon_{s}^{p}\right) - \frac{4}{3}\frac{s_{us,p}}{\varepsilon_{s,r}^{p}}\|\Delta\boldsymbol{e}^{p}\| \\ = 2G\|\boldsymbol{e}^{e,A} + \Delta\boldsymbol{e}\| - 2G\|\Delta\boldsymbol{e}^{p}\| \\ \rightarrow \|\Delta\boldsymbol{e}^{p}\| = \frac{2G\|\boldsymbol{e}^{e,A} + \Delta\boldsymbol{e}\| - \sqrt{\frac{2}{3}}d\left(\varepsilon_{s}^{p}\right)}{2G - \frac{4}{3}\frac{s_{us,p}}{\varepsilon_{s,r}^{p}}} \end{aligned} \tag{10}$$

Alternatively, it can be determined by forcing the deviatoric stress at state B (q^{B}) to fall at the reduced yield surface, by

$$q^{B} = q^{T} - 3G\Delta\varepsilon_{s}^{p} = d\left(\varepsilon_{s}^{p}\right) - \frac{\Delta\varepsilon_{s}^{p}}{\varepsilon_{s,r}^{p}}2s_{u,p} \rightarrow \Delta\varepsilon_{s}^{p} = \frac{q^{T} - d\left(\varepsilon_{s}^{p}\right)}{3G - 2\frac{s_{u,p}}{\varepsilon_{s,r}^{p}}} \tag{11}$$

where $q^{T} = 2\sqrt{\frac{3}{2}}G\left\|\boldsymbol{e}^{\boldsymbol{A}} + \Delta\boldsymbol{e}\right\|$ is the deviatoric stress at the virtual state T. The elastic strain tensor at the new state B is therefore

$$\boldsymbol{e}^{e,B} = \left(\boldsymbol{1} - \frac{\|\Delta\boldsymbol{e}^{p}\|}{\|\boldsymbol{e}^{A} + \Delta\boldsymbol{e}\|}\right)\left(\boldsymbol{e}^{e,A} + \Delta\boldsymbol{e}\right) \tag{12}$$

The stress tensors can then be fully solved through equations (4) to (7).

Non-negative value of incremental plastic strain requires

$$2G - \frac{4}{3}\frac{s_{us,p}}{\varepsilon_{s,r}^{p}} > 0 \rightarrow s_{us,p} < \frac{3}{2}G\varepsilon_{s,r}^{p} \tag{13}$$

The physical meaning of inequality (13) is that the softening rate $\frac{s_{\mathrm{u,p}}}{\gamma_{\mathrm{r}}^{\mathrm{p}}}$ should be less than the unloading shear modulus; otherwise, the portion of plastic shear strain transferred from the initially elastic part (due to softening) may self-drive the softening process. Therefore, if inequality (13) is not satisfied, the shear strength would be essentially reduced to the residual even with little plastic deformation.

Shear stress at weak layer

Within the slip surface, the shear stress (τ_{w}) is limited to the current shear strength, which is reduced during shearing, and given by

$$\tau_w = s_{uw}(\delta^p) = max\left(1 - \frac{\delta^p}{\delta_r^p}, \quad \frac{1}{S_t}\right) \cdot s_{uw,p} \tag{14}$$

where $\delta^{\mathrm{p}} = \int_0^t \left\| \dot{\boldsymbol{\delta}}^{\mathrm{p}} \right\| dt$ is the accumulated plastic shear displacement across the weak layer, $\delta_{\mathrm{r}}^{\mathrm{p}}$ the value of δ^{p} at the residual shear stress, and $s_{\mathrm{uw,p}}$ the peak undrained shear strength in the weak layer. Ignoring displacement beneath the weak layer (Zhang et al. 2015), the horizontal slide displacement can be related to the shear displacement across the weak layer by $\frac{u}{\cos\theta} = \delta = \delta^{\mathrm{e}} + \delta^{\mathrm{p}}$ where θ is the slope angle and δ^{e} and δ^{p} the elastic and plastic portion of the shear displacement, respectively.

Soils surrounding the slip surface are first mobilized elastically before reaching the yield stress governed by equation (8), and the shear stress is increased to be larger than the initial value caused by gravity. Considering a linear and isotropic elasticity model, the pre-peak shear stress can be expressed by

$$\boldsymbol{\tau}_w = K\boldsymbol{\delta}^e \tag{15}$$

where K is the shear stiffness.

Figure 3b gives details of the constitutive model for weak layer soils in the $\tau_{\mathrm{w},x} - \tau_{\mathrm{w},y}$ plane, where the strain softening behaviour is isotropic, i.e., reduction of shear strength in the *x*-axis results in the same-magnitude reduction in the *y*-axis. Similar to equation (10), the incremental plastic shear displacement can be given by

$$K\|\boldsymbol{\delta}^{e,A}+\Delta\boldsymbol{\delta}\|-K\|\Delta\boldsymbol{\delta}^{p}\|=s_{uw}(\delta^{p})-\frac{s_{uw,p}}{\delta_r^p}\|\Delta\boldsymbol{\delta}^{p}\|\rightarrow\|\Delta\boldsymbol{\delta}^{p}\| =\frac{K\|\boldsymbol{\delta}^{e,A}+\Delta\boldsymbol{\delta}\|-s_{uw}(\delta^{p})}{K-\frac{s_{uw,p}}{\delta_r^p}} \tag{16}$$

Again, a non-negative value of $\|\Delta\boldsymbol{\delta}^{\mathrm{p}}\|$ requires

$$K-\frac{s_{uw,p}}{\delta_r^p}>0\rightarrow s_{uw,p}<K\delta_r^p \tag{17}$$

Otherwise, the shear strength could be immediately reduced to the residual upon any small plastic deformation.

The updated elastic shear displacement is therefore

$$\boldsymbol{\delta}^{e,B}=\left(1-\frac{\|\Delta\boldsymbol{\delta}^{p}\|}{\|\boldsymbol{\delta}^{e,A}+\Delta\boldsymbol{\delta}\|}\right)(\boldsymbol{\delta}^{e,A}+\Delta\boldsymbol{\delta}) \tag{18}$$

and the weak layer stress (vector) can then be updated through equation (15).

Gravity and drag shear stresses

The gravity shear stress is given by

$$\tau_g=\gamma' h\sin\theta \tag{19}$$

where γ' is the submerged unit weight of soil.

Hydrodynamic pressure drag for a streamlined body like a submarine sliding mass is less significant than the skin friction drag, and the latter can be approximated by (Norem et al. 1990, Elverhoi et al. 2005)

$$\tau_{drag}=\frac{1}{2}C_f\rho_w v^2;\; C_f=\left(1.89+1.62\,log\frac{L}{k}\right)^{-2.5} \tag{20}$$

where C_{f} is the frictional drag coefficient, ρ_{w} is the seawater density, L is the sliding mass length and k is the roughness length of the sliding mass surface in the range of 0.01–0.1 m. For a length of the sliding mass varying between 10 and 1000 m, the friction drag coefficient falls in the range of 0.005–0.016.

Finite volume scheme

Two layers of fixed meshes with the same mesh size and alignment were taken, as shown in Figure 4a, with the top layer used for solving mass and momentum conservation equations and the bottom layer tracking the changes in soil properties in the weak layer during slip surface growth. A finite volume method with staggered grids, as shown in Figure 4b, was used to integrate and solve the governing equations (1) to (3).

Let us consider a slope of a rectangular space domain Ω: $(0, L_x) \times (0, L_y)$ and a time interval $(0, T)$. Dirichlet boundary conditions, i.e., $u = 0$ and $v = 0$, are prescribed representing unaffected remote regions. The space domain is meshed with a grid of $N_x \times N_y$ cells, and the cells of dimensions Δx and Δy are indexed by (i, j) where $i \in (0, N_x)$ and $i \in (0, N_y)$. The centres of the bottom, top, left, and right edges of the cell (i, j) are denoted by $\left(i, j - \frac{1}{2}\right)$, $\left(i, j + \frac{1}{2}\right)$, $\left(i - \frac{1}{2}, j\right)$, and $\left(i + \frac{1}{2}, j\right)$, respectively. The mass conservation is integrated and solved over the cell, with the thickness of the sliding layer, h, and slope angle (topography), θ, discretised at the cell centre. The velocity in the *x*-direction is discretised at the centre of the edges normal to the *x*-direction, while the velocity in the *y*-direction is discretised at the centre of the edges normal to the *y*-direction. The approximation of h at cell (i, j) and time t^n is denoted by $h_{i,j}^n$. The approximation of u at the edge $\left(i + \frac{1}{2}, j\right)$ and time t^n is denoted by $u_{i+\frac{1}{2},j}^n$ while the approximation of v at the edge $\left(i, j + \frac{1}{2}\right)$ and time t^n is denoted $v_{i,j+\frac{1}{2}}^n$.

At time t^{n+1}, the mass conservation equation (1) is discretised as

$$h_{i,j}^{n+1} - h_{i,j}^{n} = \frac{\Delta t}{\Delta x}\left(qx_{i-\frac{1}{2},j}^{n} - qx_{i+\frac{1}{2},j}^{n}\right) + \frac{\Delta t}{\Delta y}\left(qy_{i-\frac{1}{2},j}^{n} - qy_{i+\frac{1}{2},j}^{n}\right) \tag{21}$$

where

$$\begin{aligned} qx_{i-\frac{1}{2},j}^{n} &= \hat{h}_{i-\frac{1}{2},j}^{n} u_{i-\frac{1}{2},j}^{n},\ \hat{h}_{i-\frac{1}{2},j}^{n} = \begin{cases} h_{i,j}^{n} & u_{i-\frac{1}{2},j}^{n} \leq 0 \\ h_{i-1,j}^{n} & u_{i-\frac{1}{2},j}^{n} > 0 \end{cases}; \\ qy_{i,j-\frac{1}{2}}^{n} &= \hat{h}_{i,j-\frac{1}{2}}^{n} v_{i,j-\frac{1}{2}}^{n},\ \hat{h}_{i,j-\frac{1}{2}}^{n} = \begin{cases} h_{i,j}^{n} & v_{i,j-\frac{1}{2}}^{n} \leq 0 \\ h_{i,j-1}^{n} & v_{i,j-\frac{1}{2}}^{n} > 0 \end{cases} \end{aligned} \tag{22}$$

The momentum conservation in the *x*-direction, i.e., equation (2), is discretised as

$$\begin{aligned} & h_{i+\frac{1}{2},j}^{n+1} u_{i+\frac{1}{2},j}^{n+1} - h_{i+\frac{1}{2},j}^{n} u_{i+\frac{1}{2},j}^{n} \\ &\quad = \frac{\Delta t}{\Delta x}\left(qx_{i,j}^{n}\hat{u}_{i,j}^{n} - qx_{i+1,j}^{n}\hat{u}_{i+1,j}^{n}\right) \\ &\quad + \frac{\Delta t}{\Delta y}\left(qy_{i+\frac{1}{2},j-\frac{1}{2}}^{n}\hat{u}_{i+\frac{1}{2},j-\frac{1}{2}}^{n} - qy_{i+\frac{1}{2},j+\frac{1}{2}}^{n}\hat{u}_{i+\frac{1}{2},j+\frac{1}{2}}^{n}\right) \\ &\quad + \frac{\Delta t}{\rho \Delta y}\left(\tau_{xy,i+\frac{1}{2},j+\frac{1}{2}}^{n} h_{i+\frac{1}{2},j+\frac{1}{2}}^{n} - \tau_{xy,i+\frac{1}{2},j-\frac{1}{2}}^{n} h_{i+\frac{1}{2},j-\frac{1}{2}}^{n}\right) \\ &\quad + \frac{\tau_{w,i+\frac{1}{2},j}^{n} + \tau_{g,i+\frac{1}{2},j}^{n} + \tau_{drag,i+\frac{1}{2},j}^{n}}{\rho} \end{aligned} \tag{23}$$

where

$$h^n_{i+\frac{1}{2},j} = \frac{h^n_{i,j} + h^n_{i+1,j}}{2};$$

$$qx^n_{i,j} = \frac{qx^n_{i-\frac{1}{2},j} + qx^n_{i+\frac{1}{2},j}}{2}, \hat{u}^n_{i,j} = \begin{cases} u^n_{i+\frac{1}{2},j} & qx^n_{i,j} \leq 0 \\ u^n_{i-\frac{1}{2},j} & qx^n_{i,j} > 0 \end{cases};$$

$$qy^n_{i+\frac{1}{2},j-\frac{1}{2}} = \frac{qy^n_{i,j-\frac{1}{2}} + qy^n_{i+1,j-\frac{1}{2}}}{2}, \hat{u}^n_{i+\frac{1}{2},j-\frac{1}{2}} = \begin{cases} u^n_{i+\frac{1}{2},j} & qy^n_{i+\frac{1}{2},j-\frac{1}{2}} \leq 0 \\ u^n_{i+\frac{1}{2},j-1} & qy^n_{i+\frac{1}{2},j-\frac{1}{2}} > 0 \end{cases}; \tag{24}$$

$$\tau^n_{xy,i+\frac{1}{2},j+\frac{1}{2}} h^n_{i+\frac{1}{2},j+\frac{1}{2}} = \frac{\tau^n_{xy,i,j} h^n_{i,j} + \tau^n_{xy,i+1,j} h^n_{i+1,j} + \tau^n_{xy,i,j+1} h^n_{i,j+1} + \tau^n_{xy,i+1,j+1} h^n_{i+1,j+1}}{4}$$

The momentum conservation in the *y*-direction, i.e., equation (3), can be discretised in a similar way.

Changes in soil properties during the landslide process are treated differently in the two layers. The soil properties, such as stress and strength, in the weak layer are updated in the fixed mesh scheme based on the current values of h, u and v, assuming that the weak layer does not move with the sliding layer. As the sliding layer moves during the landslide process, its soil properties are updated at the deformed cell centre (based on current values of u and v) and interpolated to the original fixed centre after each time increment, in the spirit of the Arbitrary Lagrangian-Eulerian method. To this end, the numerical scheme proposed here is hereafter called the Lagrangian-Eulerian depth integrated method (LEDIM).

Verification

A series of 2D landslides with 1D slip surface growth along a weak layer, studied in Zhang et al. (2019), were re-simulated using the proposed numerical scheme to verify its accuracy. The governing equations are tailored to fit for the 2D problems by ignoring the momentum in the *y*-direction (assuming the slide mass travels in the *x*-direction) and considering only one row of cells (assuming the problem is of plane strain nature). The numerical results from the proposed numerical scheme are compared with the observations from the large deformation finite element (LDFE) modelling by Zhang et al. (2019).

A curvilinear slope model composed of an overlying layer and a weak layer was used, as shown in Figure 5a. The weak layer is parallel to the slope surface and antisymmetric about the slope centre, which is set as the origin of the coordinate system. The weak layer geometry is described by

$$z = \begin{cases} -H\left[1 - exp\left(\frac{y}{H}tan\,\theta_c\right)\right], & y < 0 \\ H\left[1 - exp\left(-\frac{y}{H}tan\,\theta_c\right)\right], & y \geq 0 \end{cases} \tag{25}$$

where θ_c is the maximum slope angle at the centre, and H is the half-height of the slope.

The length of the model was set to 8,000 m so that the slope angles at two ends approach zero. The soil properties are the same as those in Zhang et al. (2019) and are listed in Table 1. For a curvilinear slope, plastic deformation is initiated at the steepest point once the maximum gravity shear stress exceeds the peak undrained shear strength, and may be followed by catastrophic propagation of the slip surface along the weak layer, which stops only when the propagating region reaches a flat part of the slope. In the benchmark cases, the peak undrained shear strength of the weak layer soil is fixed at $s_{\mathrm{uw,p}} = 10$ kPa, which is small enough to achieve catastrophic slip surface growth along the weak layer, according to the criterion of Zhang et al. (2015). The undrained shear strength of the sliding layer, however, varies between $s_{\mathrm{us,p}} = 10$, 20, 30 and 100 kPa, to simulate different post-failure behaviours.

For $s_{\mathrm{us,p}} = 100$ kPa, the sliding layer is strong enough to remain stable, with the failure concentrated within the weak layer only. The evolution of the length of the slip surface is shown in Figure 5b for both LEDIM and LDFE modelling. The slip surface firstly increases at a rate up to 70 m/s (almost double the compression wave velocity $\sqrt{E_{\mathrm{ps}}/\rho} = 37$ m/s as it propagates in both upward and downward directions) and stops with a final length of 2,350 m. The results from the two numerical methods compare well overall, although the growth of the slip surface is slightly slower and the final slip surface length is about 2% higher in the LDFE analysis. This validates the accuracy of the proposed method in simulating the slip surface growth in the weak layer.

For the other three cases with $s_{\mathrm{us,p}} = 10,\ 20$ and 30 kPa, active and passive failure are apparent at the upslope and downslope portion of the slope, respectively, as shown in Figure 6. Figure 6 also compares the upslope and downslope segments of the slip surface in the weak layer at the final stage according to the two numerical methods. With $s_{\mathrm{us,p}} = 10$ kPa, the upper layer soils are soft and flow downward after the global slab failure, with the layer becoming thinner upslope and thicker downslope. The relative strong sliding layer with $s_{\mathrm{us,p}} = 20$ and 30 kPa leads to break-up of the layer and a main scarp somewhere upslope. The proposed numerical method can generally simulate the same post-failure behaviours as the LDFE method, which further validates the method in modelling global failure.

The LDFE method is rather inefficient in simulating a 3D landslide process because of current computational capacity and the difficulty in treating a highly distorted slope surface. The proposed numerical method has a particular advantage in computational efficiency which enables it to simulate the evolution of a 3D translational landslide in sensitive soils, as will be demonstrated in the remainder of the paper.

INITIATION AND STABLE GROWTH OF SLIP SURFACE

Four types of submarine slopes (planar, S-shape, convex, and concave, as shown in Figure 7) with a sensitive marine sediment are used to study the 3D landslide evolution. All of them consist of a continental shelf, a continental slope, and a continental rise from nearshore to deep sea, with an overlying layer, a weak layer, and a base. An initial slip surface was assumed to occur within the weak layer at the centre of the continental slope. The continental slope is assumed to have an average inclination of 6° to horizontal, and the continental shelf and continental rise are horizontal. Investigations of slip surface growth and slab failure initiation focus on the planar continental slope, which is assumed sufficiently long (8,000 m) and wide (6,000 m). The complete landslide evolution, including the post-failure behaviours and the arrest of mass transport deposit, is then simulated with considerations of the full slope model and different 3D slope geometries. Although the model is tailored to fit submarine conditions, the results are expected to be robust for similar onshore conditions as well.

A local Cartesian coordinate system *x*-*y*-*z* is used, with the origin set at the slope centre and the *z*-axis pointing away from the seabed as shown in Figure 7. The expression of the planar slope geometry is straightforward with the coordinate z linearly varying from the slope crest to the toe. To describe the S-shape slope geometry, the exponential function (25), extending through the *x*-axis, is used. The convex and concave slope geometries are constructed from a truncated cone and expressed, in terms of a global Cartesian coordinate system *X*-*Y*-*Z* as shown in Figure 7c and d, by

$$Z = 2H\left(1 - \frac{\sqrt{X^2 + Y^2} - R_t}{R_b - R_t}\right) \tag{26}$$

and

$$Z = 2H\frac{\sqrt{X^2 + Y^2} - R_b}{R_t - R_b} \tag{27}$$

where R_t and R_b are radii of circular cross sections of the truncated cone through the slope crest and the slope toe, respectively. The local coordinates can then be easily related to the global coordinates based on the origin shifting as shown in Figure 7c and d.

The planar slope model is used for the in depth investigation of the evolution of the translational landslide in sensitive soils, which is followed by an initial insight into the 3D slope geometry effects considering all mentioned slope types.

Initiation of slip surface

Many large-scale landslides might be initiated in a local region (slip surface), followed by extensive growth of the slip surface and eventually global slab failure. The initial local slip surface occurs where the permanent or transient driving force exceeds the resistance. It forms either because of an increase in the driving force, e.g., by seismic events or diapirs, or a decrease in shear strength, e.g., by soil degradation or accumulation of pore pressures.

In this first study, it is sufficient to assume the initiation slip surface is symmetric, and its boundary can be described by a series of functions:

$$\left|\frac{2x}{l_x}\right|^n + \left|\frac{2y}{l_y}\right|^n = 1 \tag{28}$$

where n is a shape parameter, and l_x and l_y are dimensions of the slip surface in the *x*- and *y*-directions, respectively. The value of n is larger than unity for a convex slip surface. For n = 1 and 2, the boundary of the slip surface is a rhombus and an ellipse, respectively. As *n* increases, the pre-softened zone extends further and further outward, and as $n \rightarrow \infty$, the boundary becomes rectangular. For most cases studied here, the value of n was taken as 2. The shear strength in the initial slip surface might be reduced from the peak to the residual by slip weakening, time weakening or both, although the process may take a long time. Therefore, it is sufficient and conservative to assume that the shear strength in the slip surface has been reduced to the residual.

The force imbalance from the slip surface can be transferred and sustained by surrounding soils, which may undergo plastic failure and fall into the post-peak strain softening state. Figure 8 shows the contour of shear strength after the formation of a circular slip surface ($n = 2$, and $l_x = l_y = 40$ m), as calculated by using the proposed numerical scheme. At the initial state, the undrained shear strength is reduced to the residual at the slip surface while being maintained at the peak elsewhere. Other properties of the numerical model and materials are listed in Table 2. After the initiation of the slip surface, force transfer and re-stabilisation is simulated using the proposed numerical scheme. Within the weak layer, three zones can be identified as shown in the figure: the intact zone (where soils remain intact), the 'process zone' (where soils undergo strain softening, and shear strength ranges between the peak and the residual) and the slip surface (where soils reach the residual state). Six cross sections, three in each (x- or y-) direction, are chosen to further observe the distribution of the shear strength within the three zones, as given in Figure 8b and c. For the x-I, x-II, y-I and y-II sections which cross all three zones, discontinuities in the distributions of the shear strength exist, dropping from a post-peak value to the residual. These distinguish the process zone from the initial slip surface. The x-III and y-III profiles, however, cross the process zone and intact zone only, and the discontinuity in shear strength distribution is absent. Note that, in this case, the process zone is developed to fully resist the unbalanced forces from the slip surface, and hence the slope remains stable. This is defined as stable slip surface growth and will be detailed in the next sub-section.

Stable growth of slip surface

Figure 9 shows under what conditions a process zone might be initiated and developed. For a relatively large slip surface (i.e., $l_x = 40$ m for a circular slip surface), it can disturb and weaken adjacent soils, leading to the development of a process zone surrounding the slip surface. However, if the slip surface is sufficiently small (e.g., $l_x = 20$ m), the driving force from the slip surface might be easily sustained by the surrounding soils without the formation of the process zone, i.e., the soils remain intact as shown in Figure 9. When the diameter of the slip surface grows to $l_x = 30$ m, the process zone appears only at the front and rear of the slip surface.

The above observation reveals that: 1) for a circular slip surface, the process zone firstly emerges at the rear and in front of the slip surface; and 2) the larger the slip surface, the more significant the process zone. Figure 9 also compares the shear stress contours resulting from different sizes of slip surface. The shear stress remains the gravity value (≈6 kPa for parameters listed in Table 2) and increases to the peak at the interface between the intact and process zones. It is limited to the shear strength within the process zone and the slip surface.

Stability can be eventually achieved for the cases of $l_x = 20$, 30 and 40 m despite the development of the process zone. As defined above, the process of extensive expansion of the slip surface up to $l_x = 40$ m can be termed stable slip surface growth. In contrast, for the case of $l_x = 50$ m, the growth of the slip surface cannot be restricted under existing forces and hence is termed unstable slip surface growth. Note that Figure 9 shows a transient moment of this case, and the dynamic expansion of the slip surface during unstable slip surface growth will be discussed in the next section.

The pattern of stable growth of the slip surface depends on the shape of the initial slip surface. Figure 10 shows the different patterns of stable slip surface growth for elliptical slip surfaces with different ratios of major and minor axes, in terms of the shear strength contour. Similar to Figure 8b and c, Figure 11 presents the distributions of shear strength along the major and minor axes of the slip surface to visualise the growth pattern of the slip surface. In all cases, the stable growth of the slip surface together with the development of the process zone is obvious. As demonstrated above, for a circular slip surface with $l_x/l_y = 1$, the travel direction (*x*-direction) is the favoured direction for slip surface growth. The favoured direction along the *x*-direction of growth is enhanced with a larger axis ratio (a wider slip surface), e.g., $l_x/l_y = 2$. For a slender slip surface (of small axis ratio, $l_x/l_y = 0.25$), however, the slip surface tends to propagate along the *y*-direction first, presenting a different growth pattern from wide slip surfaces. For instance, with $l_x = 20$ m and $l_y = 60$ m, soil at the two sides of the slip surface begins to soften while the soil in front and at the rear of the slip surface remains intact. With the axis ratio $l_x/l_y = 0.5$, the slip surface seems to grow simultaneously along the periphery of the slip surface without an obvious favoured direction, which forms the most pessimistic situation.

Figure 12 briefly illustrates the three modes. The growth of the slip surface along the x-direction is driven by the compression force downslope and extension force upslope, akin to the in-plane shear mode of crack propagation in fracture mechanics (i.e., a shear stress acting parallel to the plane of the slip surface and perpendicular to the slip surface front); while the growth along the y-direction is driven by the shear force, akin to the out-of-plane shear mode of crack propagation in the fracture mechanics (i.e., a shear stress acting parallel to the plane of the slip surface and parallel to the slip surface front). Here, the former is defined as the compression-extension mode and the latter is defined as the shear mode. In reality, a combined mode including both the compression-extension and shear modes is expected to be more common, particularly when the slip surface growth is unstable and continuous, as will be discussed in the next sub-section. It has not been possible to study the shear and combined modes in previous 2D investigations (e.g., Puzrin et al. 2004, Kvalstad et al. 2005, Zhang et al. 2015).

UNSTABLE GROWTH OF SLIP SURFACE

Unstable slip surface growth mechanism

With an initial slip surface of $l_x = l_y = 50$ m and other properties listed in Table 2, the growth of the slip surface is unstable and can only be limited by slope flattening or global slab failure. Figure 13a, b and c, respectively, shows the evolution of the shear strength contour, horizontal velocity field and vertical velocity field during the unstable growth of the slip surface. To intensively investigate the slip surface growth without slab failure, the shear strength in the overlying layer was intentionally set to a high value (1,000 kPa). At $t = 10$ s, the slip surface grows from a circle to an ellipse with the major axis parallel to the potential travel direction in the compression-extension mode. Thereafter, the slip surface grows dramatically in the combined mode and propagates more outward at the four shoulders, forming a distinctive ‘peanut’ shape at $t = 25$ s. The wide shoulders are generated because of larger horizontal velocity in these areas, whereas along the major (y-) and minor (x-) axes of the slip surface, the horizontal velocity is close to zero, as shown in Figure 13b. The slip surface is symmetric in terms of both x- and y-axes before $t = 50$ s. At $t = 50$ s, however, the downslope part of the slip surface is slightly larger than the upslope, as soil begins to be accumulated more downslope with downward movement of the slide mass.

Zhang et al. (2020) assumed that the (horizontal) velocity of the slide mass along the x-direction is negligible compared to the y-direction component, which has been found to be a robust result during the stable growth of slip surface through LDFE modelling. This generates a plane strain condition with the compression/extension modulus in the sliding layer calculated by

$$E_{ps} = \frac{E}{1 - \nu^2} = \frac{2G}{1 - \nu} \tag{29}$$

where E is the Young’s modulus and ν the Poisson’s ratio. This assumption needs to be verified for the stage of unstable slip surface growth. To achieve this, conservation of momentum in the x-direction, i.e. governing equation (2), was ignored and the horizontal component of the velocity was set to zero. Numerical results of such an idealised case in terms of the strength contours are presented in Figure 13d. For $t = 5$ s and 10 s, the slip surfaces of the idealised case are almost identical to the case formulated by rigorous governing equations as shown in Figure 13a. However, with further unstable growth of the slip surface, the shape of the slip surface remains an ellipse, which is different from the ‘peanut’ shape of the rigorous case.

Figure 14 compares the two mechanisms at $t = 50$ s. The major and minor axes of the ‘peanut’ slip surface are the same as those of the 'ellipse' slip surface, with the area of the slip surface larger in the former mechanism. The different mechanisms found in the two cases imply that the horizontal movement of the slide mass plays an important role and has to be considered during the unstable growth of the slip surface.

Unstable slip surface growth speed

Once a slip surface falls into the unstable growth stage, the growth speed depends on how the unbalanced forces are transferred within the overlying layer. For the compression-extension mode, the growth of the slip surface is driven by the compressional/tensile force, and therefore the growth speed (of the major axis) can be related to the compression wave velocity

$$v_{maj} = 2\sqrt{\frac{E'}{\rho}} \tag{30}$$

where E' is the compression modulus. Note that the number 2 in the expression means that the growth speed is double the wave velocity, as the slip surface grows in both the upslope and downslope directions. Similarly, for the shear mode, the growth speed of the minor axis can be related to the shear wave velocity

$$v_{min} = 2\sqrt{\frac{G}{\rho}} \tag{31}$$

For plane strain and undrained conditions, the compression modulus, $E' = E_{\mathrm{ps}}$, is four times the shear modulus (see equation (29)) and therefore, the major axis always doubles the minor axis of the slip surface. This can be seen in Figure 14, where the major axes of the slip surfaces are almost 3,000 m while the minor axes are around 1,500 m in both mechanisms.

Figure 15a shows the length (major axis) and width (minor axis) of the slip surface during its growth for the selected case, compared with the analytical solutions given by equations (30) and (31). It should be noted that the growth of the slip surface evolves from the stable to unstable stages with the transition emerging at around $t = 4$ s. During the stable growth stage, both axes of the slip surface are assumed unchanged. With this idealisation, the growth of the two axes of the slip surface in the numerical modelling can be well predicted by the analytical solutions, with the growth speeds being 34 m/s and 68 m/s for the major and minor axes, respectively. Such fast speeds reveal that unstable growth of the slip surface is catastrophic.

Figure 15b gives the area of the slip surface during its unstable growth for both mechanisms. For the 'ellipse' mechanism, the area can be calculated exactly by

$$A = \frac{\pi}{4} l_x l_y \tag{32}$$

which is shown by the good agreement between the numerical and analytical results in the figure. The area of the ellipse slip surface is initially 1,962.5 m^2 and increases to 3.6 km^2 in 50 s. The peanut slip surface (5.3 km^2) is about 45% larger than the ellipse slip surface at $t = 50$ s. The fast growth of the slip surface implies that during an earthquake, even with a short period of shaking, a large slip surface with a magnitude of ~ km^2 might be formed. Such a large slip surface may further result in global slab failure and debris flow. Therefore, it is key to determine in what conditions the slip surface can grow unstably, which will be discussed in the next section.

Criteria for unstable growth of slip surface

For a slip surface described by a series of functions (28), the area of the slip surface can be calculated by

$$A = \frac{l_x l_y}{n} \cdot \frac{\Gamma(1 + 1/n)\Gamma(1/n)}{\Gamma(1 + 2/n)} \tag{33}$$

where Γ is the gamma function. By integrating the normal and shear resistances along the boundary of the slip surface, one may calculate the total resistance and compare it to the driving force from the slip surface, whereby the critical area of the slip surface for unstable growth is given by (Zhang et al. 2020)

$$A_{cri} = 32\left(\frac{1-r}{r}l_c\right)^2 \tag{34}$$

where r is the shear stress ratio and l_c is the critical length relevant to the process zone size, given by

$$r = \frac{\tau_g - s_{uw,r}}{s_{uw,p} - s_{uw,r}}, l_c = \sqrt{\frac{Gh\delta_r^p}{s_{uw,p} - s_{uw,r}}} \tag{35}$$

For static analysis, ignoring any inertia effects, the criterion (34) is conservative compared to the numerical data from finite element and finite difference modelling (Zhang et al. 2020).

A parametric study was conducted to observe the effects of the shape parameter, n, and the dimensions of the slip surface on the critical area for unstable slip surface growth. The gravity loads and the critical surface areas at critical conditions for all cases are presented in Table 3. Figure 16a shows a comparison of the numerical results with or without inertia effects and the analytical results by criterion (34). In dynamic analysis conducted in the current study, the critical area estimated by (34) is not always conservative, particularly with a large shear stress ratio. Assuming that the dynamic criterion meets the same series of functions as the static criterion (34), the best fit of the numerical data from the dynamic analysis gives

$$A_{cri} = 18.4\left(\frac{1-r}{r}l_c\right)^2 \tag{36}$$

which is shown in Figure 16b. This means that the critical area of the slip surface for unstable slip surface growth under dynamic conditions is on average 42.5% smaller than that ignoring inertia effects. This echoes the finding that in a 2D plane strain slope, the critical length (major axis) of slip surface for catastrophic propagation can be up to 50% lower with inertia effects than without inertia effects (Zhang et al. 2016). Extending this observation to the 3D case, one may simply assume for the dynamic unstable growth a 50% reduction in the critical area of the slip surface from the static criterion (36), that is

$$A_{cri} = 16\left(\frac{1-r}{r}l_c\right)^2 \tag{37}$$

Figure 16a shows that the criterion (37) gives estimates of the critical slip surface area well below the numerical data and is therefore conservative.

SLAB FAILURE AND POST-FAILURE BEHAVIOURS

Slab failure

Growth of the slip surface within the weak layer and slab failure within the overlying layer are two competing mechanisms leading to large-scale landslides in sensitive soils. The extent of the slip surface depends on how ‘weak’ the weak layer is. With the growth of the slip surface, the driving force increases, and so does the deviatoric stress within the overlying layer given by equations (7) and (8). Therefore, at a certain stage of the unstable slip surface growth, the overlying soils may reach the maximum allowable deviatoric stress, initiating slab failure.

Figure 17 shows the increase of the maximum deviatoric stress of the overlying soils with the growth of the slip surface. Note that the at-rest lateral earth pressure coefficient, which is the horizontal earth pressure over the vertical earth pressure, was set to $K_0 = 0.5$ for all numerical cases evolving into slab failure. The peak undrained shear strength of the weak layer soil was fixed at $s_{\mathrm{uw,p}} = 10$ kPa, while the strength of the overlying soil, $s_{\mathrm{us,p}}$, was varied between 10 kPa, 20 kPa, 50 kPa, 100 kPa and 1,000 kPa without strain softening. The other parameters remain the same as those in Table 2. At the initial state, the deviatoric stress is 26 kPa, which is essential to make the slip surface grow unstably from an initial area of 2,352 m^2 (with $l_x =$ 40 m and $l_y = 80$ m). In the case of $s_{\mathrm{us,p}}/s_{\mathrm{uw,p}} = 100$, the ‘unrealistic’ strong overlying layer leads to the pure growth of the slip surface over the whole simulation domain (8,000 m × 6,000 m), and the deviatoric stress keeps growing, as shown in the figure. For the other cases, the deviatoric stress is limited to $2s_{\mathrm{us,p}}$, which satisfies the generalised nature of the von Mises failure criterion with respect to the Tresca failure criterion. The stronger the overlying soil, the larger the slip surface at the initiation of slab failure. For example, the slip surface at the slab failure initiation is as large as 1.1 km^2 in the case of $s_{\mathrm{us,p}}/s_{\mathrm{uw,p}} = 10$, while it is reduced by 2/3 when the undrained shear strength of the overlying soil is decreased by half.

When the weak layer is not literally 'weak', i.e., in the case of $s_{\mathrm{us,p}}/s_{\mathrm{uw,p}} = 1$, the slab failure is triggered without unstable growth of the slip surface, as the required deviatoric stress (26 kPa) is essentially higher than the maximum allowable value ($2s_{\mathrm{us,p}} = 20$ kPa). Figure 18 shows the slip surface growth with respect to the contours of the shear strength in the weak layer, and the slab failure with respect to the contours of the plastic strain and deviatoric stress in the overlying layer. At $t = 5$ s, slab failure emerges at the rear of the slip surface where soils are unloaded and the deviatoric stress reaches the maximum 20 kPa; while in front of the slip surface, soils are loaded and the deviatoric stress decreases from the initial value. At $t = 10$ s, the soils in front of the slip surface have been loaded to the passive failure state, and, accordingly, the deviatoric stress also reaches the maximum. Thereafter, the slab failure propagates mainly at the downslope portion with diffusive plastic strain; at the rear of the slip surface, the plastic strains are accumulated, and the propagation of the slab failure is not apparent. Rather than like a fan zone formed in front of the slip surface, the rear boundary of the slip surface (or the main scarp) is quite straight. For the planar slope studied here, the slip surface keeps growing along the *x*-direction, with the side boundaries of the slip surface continuing to extend further outward.

Figure 19 compares the slip surface and slab failure at $t = 50$ s for cases with different strength ratios, $s_{\mathrm{us,p}}/s_{\mathrm{uw,p}} = 1, 2, 5, 10$. For the case of the strongest overlying layer ($s_{\mathrm{us,p}}/s_{\mathrm{uw,p}} = 10$), the slab failure initiates only at the rear and the sides of the growing slip surface. With the decrease of the overlying soil strength, the downslope portion fails together with the upslope portion. The slip surface pattern of the downslope portion does not alter significantly, although the accumulated plastic strain in the overlying layer decreases with the increase of the overlying soil strength. A 'peanut' slip surface mechanism remains for $s_{\mathrm{us,p}}/s_{\mathrm{uw,p}} = 2, 5, 10$ before the slab failure; while for $s_{\mathrm{us,p}}/s_{\mathrm{uw,p}} = 1$, only the bottom half of the 'peanut' is developed as the slab failure occurs early and stops the growth of the slip surface upslope. The upper half of the slip surface, however, becomes flat and propagates less after the slab failure.

Post-failure evolution and arrest of landslide

It has been demonstrated above that, once initiated, the slip surface growth and slab failure propagation cannot be arrested on a planar slope. Either slope flattening or material strengthening can restrict slip surface growth and slab failure propagation. To further observe the arrest of slip surface and post-failure behaviours, the full slope model including a relatively flat continental shelf and a continental rise, as shown in Figure 7, is used in the remainder of the study. For the planar slope model, it consists of a continental slope with a slope angle of 6° and length of 400 m (coordinate y from −200 m to 200 m), a flat continental shelf ($y <$−200 m) and a flat continental rise ($y > 200$ m). The peak undrained shear strength of the weak layer soil, the weak layer depth and the submerged soil unit weight were chosen as $s_{\mathrm{uw,p}} = 15$ kPa, $h = 8$ m, and $\gamma' = 8$ kN/m^3, respectively. This parameter set generates a strength ratio of $s_{\mathrm{uw,p}}/\gamma' h = 0.234$, which is typical for normally consolidated submarine clay sediments. The overlying layer was assumed slightly over-consolidated with a peak strength of $s_{\mathrm{us,p}} = 10$ kPa and strength ratio of 0.31. The soil sensitivities of the weak layer and the overlying layer were set to 7 and 2, respectively. Again, an elliptical initial slip surface of $l_x = 40$ m and $l_y = 80$ m was pre-set. Other parameters are the same as those listed in Table 2.

Figure 20a shows the numerical landslide evolution from the slip surface growth, the slab failure initiation, post-failure stage and re-deposition with respect to the contours of the shear strength in the weak layer and the plastic strain in the overlying layer, and the changes in the overlying layer thickness. Note that the normalised sliding layer thickness is calculated as the ratio of the current thickness and the initial thickness of the overlying layer. At $t = 10$ s, slab failure is initiated with a certain amount of slip surface growth. The plastic strain is more concentrated at the rear of the slip surface, and a curved back scarp is formed at this stage, with the height of the scarp exceeding 4 m ($0.5h$). The main scarp moves backward with the retrogressive failure at the rear of the slip surface. The retrogression is stopped by the flat continental shelf, leaving a fairly straight main scarp of 200 m in length and over 4 m in height. Because of the strain softening, the failed overlying mass is torn apart into blocks, within which the plastic strain of the sliding layer is insignificant as shown in the second row of Figure 20a. The blocks are broken into smaller pieces and finally disappear during their downward movement. The failed and softened slide mass is finally deposited at the continental rise, forming a compressed fan zone of around 400 m in diameter and over 4 m in heave. The extent of the slip surface in the weak layer is almost identical to the combined area of the source region and deposition fan zone. Features such as the main scarp, the blocks seen during progressive failure, and the deposition fan zone are consistent with site investigations of many historical submarine landslides, e.g., the Loch Eriboll Slide discovered offshore Scotland (Carter et al. 2020) and shown in Figure 20b.

Effects of a 3D slope geometry

Three typical 3D slope types, as shown in Figure 7b, c and d, are considered in this section in order to demonstrate ability of the proposed framework to handle true 3D slope geometries and in order to gain an initial insight into the slope geometry effects on the translational landslide evolution. For the S-shape slope, the half-height of the slope in equation (25) was set to be the same as for the planar slope, i.e., $H = 21$ m, and the maximum slope angle was taken as $\theta_c =$

9° such that the average slope angle within the range of $-500\ \mathrm{m} < y < 500\ \mathrm{m}$ is equal to the planar slope angle of 6°. For the convex slope, the values of R_t and R_b were set to 800 m and 1,200 m, respectively; while for the concave slope, $R_b = 800$ m and $R_t = 1{,}200$ m. The slope angle of the convex and concave slope models is the same with the planar slope model.

Figure 21 compares the final states of the four slope models with respect to the fields of the shear strength in the weak layer, the shear stress in the weak layer, the plastic strain in the sliding layer, and the normalised sliding layer thickness. It can be noted that the far field gravity shear stress fields (second row of Figure 21) strongly depend on the geometry of the problem. The results of the planar, convex and concave slopes look very similar, with slightly more horizontal slip surface growth observed in the convex slope and slightly more retrogressive extension pertained in the concave slope, suggesting that the slope gradient along the x-direction has limited influence on the landslide evolution. In contrast, the final slip surface and mass transport deposit observed in the S-shape curvilinear slope are significantly different from the other three models with less extended retrogressive failure and a smaller fan heave zone. This confirms the conclusions from the previous studies (e.g., Puzrin et al. 2017, Zhang et al. 2021) that the slope gradient along the *y*-direction has a considerable effect on the landslide evolution.

The examples shown here mainly aim to verify the capability of the proposed numerical scheme in simulating 3D post-failure behaviours of landslides in sensitive clays. Detailed investigation of the effects of the 3D slope geometry on post-failure patterns is beyond the scope of the present work and will be explored in future studies by using the proposed numerical tool.

CONCLUSIONS

This study has simulated and discussed the whole evolution of a translational landslide in a 3D slope of sensitive soils by using an original large deformation numerical tool. A translational landslide in sensitive soils might be enormous but is often initiated by a localised failure zone within a weak layer. Much attention has been paid to understanding and quantifying the failure process of translational landslides with 2D plane strain models. Some 3D simulations of post-failure debris flow have been performed with advanced numerical methods, but few of them have examined the failure initiation. The complete 3D evolution of translational landslides in sensitive soils, including the slip surface initiation and growth along a weak layer, slab failure, post-failure behaviours and re-stabilisation, has been investigated. The numerical scheme has been established by solving governing equations in terms of the conservations of the mass and the momentum of sliding mass in discretised Eulerian cells of a simulation domain with a depth integrated finite volume method. A von Mises yield criterion with isotropic and linear strain softening has been used with a Lagrangian update of material properties at each cell centre after each simulation step. Some main findings are as follows.

- A slip surface might be formed and grow stably within a weak layer due to extensive external triggers such as earthquakes and excess pore pressure accumulation. Strain softening of sensitive soils during shearing leads to formation of a process zone, where undrained shear strength reduces from the peak towards the residual, surrounding the slip surface. For an initially wide slip surface, the process zone first emerges in front and at the rear of the slip surface, whereas for an initially slender slip surface, it occurs at the two sides. For an elliptical slip surface, the process zone develops around the periphery of the slip surface without any favoured direction.
- Once the slip surface reaches a certain size, its growth becomes unstable and catastrophic, restricted only by slope flattening or slab failure. The critical area of the slip surface for unstable growth is almost independent of its shape but depends on the material properties and shear stress ratio over the slip surface. For planar slides, it is

given by $A_{\mathrm{cri}} = 16\left(\frac{1-r}{r} l_{\mathrm{c}}\right)^2$ where the shear stress ratio, r, and characteristic length, l_{c}, are expressed by equation (35).

- Regardless of the initial shape, the slip surface transitions from an ellipse to a 'peanut' pattern during the unstable growth stage, with expansion rates equal to compression wave velocity and shear wave velocity along the major and minor axes of the slip surface, respectively. Within the sliding layer, the unbalanced force is transferred from the slip surface to the surrounding soils, leading to unloading upslope and loading downslope. Deviatoric stress increases with the expansion of the slip surface until it reaches the maximum value controlled by the undrained shear strength. The global slab failure usually initiates at the rear of the slip surface if the at-rest earth pressure coefficient is smaller than unity. The stronger the overlying layer, the larger the slip surface before the global slab failure. After the slab failure, the growth of the slip surface is in alignment with the propagation of the slab failure.
- A main scarp forms at the rear of the slip surface after the slab failure, and is followed by retrogression, which is limited by upslope slope flattening. The failed slide mass disintegrates into blocks and then turns to fully softened debris flow with downward movement. The slide mass finally re-deposits at the flat terrain with the mass transport deposit forming a fan zone. There differences in the landslide failure extension and mass transport deposit morphology between the planar, the convex, and the concave slopes of the same and uniform slope angle and parallel layering characteristic of sediments were found to be insignificant. In contrast, in the curvilinear slope, a significantly less extended failure upslope and a smaller fan heave zone downslope have been observed.

The numerical results obtained have allowed us to quantify the unstable growth of the slip surface and slab failure initiation. Though the diverse post-failure mechanisms are yet to be fully understood and quantified, the numerical scheme has shown its potential to simulate 3D post-failure behaviours in 3D slope geometries following different initiation histories. However, the constitutive model used here is only valid for fine materials under undrained conditions. The robustness of the numerical scheme with advanced constitutive models is yet to be verified. Meanwhile, the numerical scheme needs proper adjustment to fit the modelling of landslides in complex nonlinear terrains.

ACKNOWLEDGEMENTS

The authors would like to thank Prof. Mark Randolph of the University of Western Australia and Prof. Dong Wang of the Ocean University of China for valuable discussions on the topic. Data used in this study is publicly available at the Figshare repository 10.6084/m9.figshare.17029700.

REFERENCES

Biscarini, C. (2010). Computational fluid dynamics modelling of landslide generated water waves. Landslides, 7: 117–124.

Carter, G. D. O., Cooper, R., Gafeira, J., Howe, J. A. and Long, D. (2020). Morphology of small-scale submarine mass movement events across the northwest United Kingdom. Geomorphology, 365: 107282.

Cheng, Y. M. and Yip, C. J. (2007). Three-dimensional asymmetrical slope stability analysis extension of Bishop's, Janbu's, and Morgenstern–Price's Techniques. Journal of Geotechnical and Geoenvironmental Engineering, 133(12): 1544–1555.

Cornforth, D. H. (2005). Landslides in practice: investigation, analysis and remedial/preventative options in soils. John Wiley and Sons Inc., New Jersey, NJ, USA.

Dong, Y., Wang, D. and Randolph, M. F. (2017). Runout of submarine landslide simulated with material point method. Procedia Engineering, 175: 357–364.

Duncan, J. M. (1996). State of the art: limit equilibrium and finite-element analysis of slopes, Journal of Geotechnical Engineering, 122(7): 557–596.

Elverhoi, A., Issler, D., De Blasio, F.V., Ilstad., Harbitz, C.B. and T. Gauer, P. (2005). Emerging insights into the dynamics of submarine debris flows. Natural Hazards and Earth System Sciences, 5: 633–648.

Griffiths, D. V. and Marquez, R. M. (2007). Three-dimensional slope stability analysis by elasto-plastic finite elements. Géotechnique, 57(6): 537–546.

Haflidason, H., Sejrup, H. P., Nygard, A., Mienert, J., Bryn, P., Lien, R., Forsberg, C. F., Berg, K. and Masson, D. (2004). The Storegga Slide: architecture, geometry and slide development. Marine Geology, 213(1–4): 201–234.

Huang, C. C. and Tsai, C. C. (2000). New method for 3D and asymmetrical slope stability analysis. Journal of Geotechnical and Geoenvironmental Engineering, 126(10): 917–927.

Hungr, O. (1995). A model for the runout analysis of rapid slides, debris flows, and avalanches. Canadian Geotechnical Journal, 32: 610–623.

Hungr, O., Salgado, F. and Byrne, P. (1989). Evaluation of a three-dimensional method of slope stability analysis. Canadian Geotechnical Journal, 26(4): 679–686.

Issler, D., L'Heureux, J.S., Cepeda, J.M. and Quan Luna, B. (2015). Towards a numerical run-out model for quick-clay slides. EGU General Assembly 2015, held 12-17 April, 2015 in Vienna, Austria.

Klein, B. and Puzrin, A. M. (2021). Growth of slip surfaces in 3D conical slopes. International Journal for Numerical and Analytical Methods in Geomechanics, Online, https://doi.org/10.1002/nag.3220.

Kvalstad, T. J., Andresen, L., Forsberg, C. F., Berg, K., Bryn, P., Wangen, M. (2005). The Storegga slide: evaluation of triggering sources and slide mechanics. Marine and Petroleum Geology, 22(1-2): 245–256.

Lam, L. and Fredlund, D. G. (1993). A general limit equilibrium model for three-dimensional slope stability analysis. Canadian Geotechnical Journal 30(6): 905–919.

L'Heureux, J.S., Longva, O., Steiner, A., Hansen, L., Vardy, M.E., Vanneste, M., Haflidason, H., Brendryen, J., Kvalstad, T.J., Forsberg, C.F., Chand, S. and Kopf, A. (2012). Identification of weak layers and their role for stability of slopes at Finneidfjord, Northern Norway. In: Yamada Y. et al. (eds) Submarine Mass Movements and Their Consequences. Advances in Natural and Technological Hazards Research, vol 31. Springer, Dordrecht.

Lin, H. D., Wang, W. C. and Li, A. J. (2020). Investigation of dilatancy angle effects on slope stability using the 3D finite element method strength reduction technique. Computers and Geotechnics, 118: 103295.

Liu, K. F. and Huang, M. C. (2006). Numerical simulation of debris flow with application on hazard area mapping. Computational Geosciences, 10(2): 221–240.

Locat, A., Leroueil, S., Bernander, S., Demers, D., Jostad, H.P, Ouehb, L. (2011). Progressive failure in eastern Canadian and Scandinavian sensitive clays. Canadian Geotechnical Journal, 48(11): 1696–1712.

Micallef, A., Masson, D.G., Berndt, C. and Stow, D.A.V. (2007). Morphology and mechanics of submarine spreading: A case study from the Storegga Slide. Journal of Geophysical Research: Earth Surface, 112: F03023.

Morgenstern, N. and Price, V. (1965). The analysis of the stability of general slip surfaces, Géotechnique, 15(1): 79–93.

Norem H, Locat J, Schieldrop B (1990) An approach to the physics and the modelling of submarine flowslides. Marine Georesources & Geotechnology, 9(2): 93–111.

Puzrin, A.M., Germanovich, L.N. and Friedli, B. (2016). Shear band propagation analysis of submarine slope stability. Géotechnique, 66(3): 188–201.

Puzrin AM, Germanovich LN, Kim S (2004) Catastrophic failure of submerged slopes in normally consolidated sediments. Géotechnique 54(10): 631–643.

Skempton, A.W. (1985). Residual strength of clays in landslides, folded strata and the laboratory. Geotechnique, 35(1): 3–18.

Spencer, E. (1967). A method of analysis of stability of embankments assuming parallel inter-slice forces. Géotechnique, 17(1): 11–26.

Zhang, W., Klein, B., Randolph, M. F. and Puzrin, A. M. (2021). Upslope failure mechanisms and criteria in submarine landslides: shear band propagation, slab failure and retrogression. Journal of Geophysical Research: Solid Earth, Online, DOI: 10.1029/2021JB022041

Zhang, W. and Puzrin, A. M. (2021). Depth integrated modelling of submarine landslide evolution. Landslides, 18: 3063–3084.

Zhang, W., Randolph, M. F., Puzrin, A. M. and Wang, D. (2020). Criteria for planar shear band propagation in submarine landslide along weak layers. Landslides, 17(4): 855–876.

Zhang, W., Wang, D., Randolph, M. F. and Puzrin, A. M. (2015). Catastrophic failure in planar landslides with a fully softened weak zone. Géotechnique, 65(9): 755–769.

Zhang, W., Wang, D., Randolph, M. F. and Puzrin, A. M. (2016). Dynamic propagation criteria for catastrophic failure in planar landslides. International Journal for Numerical and Analytical Methods in Geomechanics, 2016, 40: 2312–2338.

Zhang, W., Randolph, M. F., Puzrin, A. M. and Wang, D. (2019). Transition from shear band propagation to global slab failure in submarine landslides. Canadian Geotechnical Journal, 56(4): 554–569.

Zhang, Y., Chen, G., Zheng, L., Li, Y. and Zhuang, X. (2013). Effects of geometries on three dimensional slope stability. Canadian Geotechnical Journal, 50(3): 233–249.

List of tables

Table 1 Parameters for benchmark case

Parameter	Value	Unit
Length of slope	8,000	m
Maximum slope angle, θ_c	6	degrees
Half slope height, H	20	m
Shear modulus, G	662.25	kPa
Shear stiffness in the weak layer, K	1656	kPa/m
At-rest earth pressure coefficient, K_0	0.75	
Gravity acceleration, g	9.81	m/s^2
Saturated density, ρ	1870	kg/m^3
Peak undrained shear strength in weak layer, $s_{uw,p}$	10	kPa
Peak undrained shear strength in sliding layer, $s_{us,p}$	10, 20, 30, 100	kPa
Soil sensitivity in weak layer	5	
Soil sensitivity in sliding layer	1	
Residual plastic shear displacement, δ_r^p	0.2	m

Table 2 Base parameters for numerical cases

Parameter	**Value**	**Unit**
Overall model length, L	4,000	m
Overall model width, B	150	m
Slope angle, θ	6.0	degrees
Sliding layer thickness, h	8.0	m
Shear stiffness in weak layer, K	1,656	kPa/m
Shear modulus in sliding layer, G	500	kPa
Peak shear strength in weak layer, $s_{uw,p}$	10	kPa
Residual shear strength in weak layer, $s_{uw,r}$	2	kPa
Plastic shear displacement to the residual strength, δ_r^p	0.2	m
Plastic shear strain to the residual strength, $\varepsilon_{s,r}^p$	0.2	
At-rest lateral earth pressure coefficient, K_0	0.5	
Characteristic length[1], l_c	10	m
Submerged soil density, ρ	740	kg/m^3

[1] $l_{\mathrm{c}} = \sqrt{\frac{Gh\delta_{\mathrm{r}}^{\mathrm{p}}}{\tau_{\mathrm{p}}-\tau_{\mathrm{r}}}}$

Table 3 Critical conditions for unstable slip surface growth by numerical analysis

Dimension of slip surface				**Gravity load**	
l_x **(m)**	l_y **(m)**	n	A **(m²)**	ρ **(kg/m³)**	r
First series: $l_y/l_x = 1,\ n = 2$					
10	10	2	79	1,170	0.943
20	20	2	314	1,070	0.841
40	40	2	1,257	870	0.637
60	60	2	2,827	730	0.494
80	80	2	5,027	640	0.403
100	100	2	7,854	580	0.341
120	120	2	11,310	540	0.301
140	140	2	15,394	500	0.260
160	160	2	20,106	470	0.229
180	180	2	25,447	450	0.209
200	200	2	31,416	430	0.189
Second series: $l_y/l_x = 2,\ n = 2$					
10	20	2	157	1,130	0.902
20	40	2	628	980	0.749
40	80	2	2,513	750	0.515
60	120	2	5,655	630	0.392
80	160	2	10,053	550	0.311
100	200	2	15,708	500	0.260
120	240	2	22,619	460	0.219
140	280	2	30,788	430	0.189
Third series: $l_y/l_x = 3,\ n = 2$					
10	30	2	236	1,090	0.862
20	60	2	942	910	0.678
40	120	2	3,770	680	0.443
60	180	2	8,482	570	0.331
80	240	2	15,080	500	0.260
100	300	2	23,562	460	0.219
120	360	2	33,929	430	0.189
Fourth series: $l_y/l_x = 0.5,\ n = 2$					
20	10	2	157	1,130	0.902
40	20	2	628	990	0.760
80	40	2	2,513	770	0.535
120	60	2	5,655	640	0.403
160	80	2	10,053	560	0.321
200	100	2	15,708	510	0.270
240	120	2	22,619	470	0.229
280	140	2	30,788	450	0.209
Fifth series: $l_y/l_x = 2,\ n = 1$					
20	40	1	400	1,040	0.811
40	80	1	1,600	830	0.596
60	120	1	3,600	700	0.464
80	160	1	6,400	610	0.372
100	200	1	10,000	550	0.311
120	240	1	14,400	510	0.270
Sixth series: $l_y/l_x = 2,\ n = 10$					
20	40	10	789	950	0.719
40	80	10	3,154	720	0.484
60	120	10	7,097	590	0.352
80	160	10	12,617	520	0.280
100	200	10	19,715	470	0.229
120	240	10	28,389	440	0.199

List of figures

thickness; (b) similar submarine landslide morphology discovered in the Loch Eriboll Slide (Carter et al. 2020)

Figure 21 3D slope geometry effect on the ultimate slip surface growth and morphology of the mass transport deposit in translational landslides

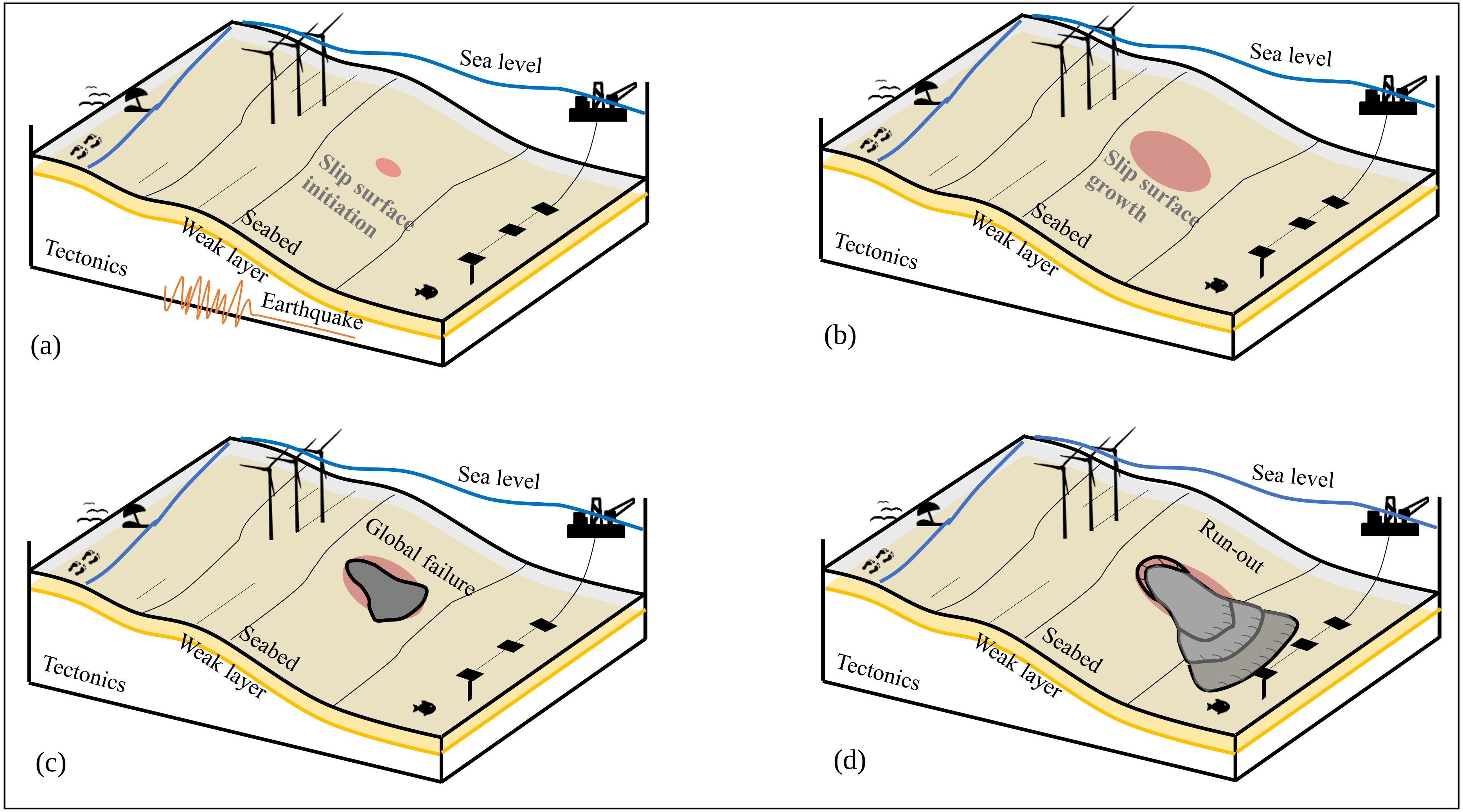

Figure 1 Conceptual evolution of submarine landslides: (a) local slip surface in weak layer; (b) slip surface growth; (c) global slab failure; (d) post-failure behaviour

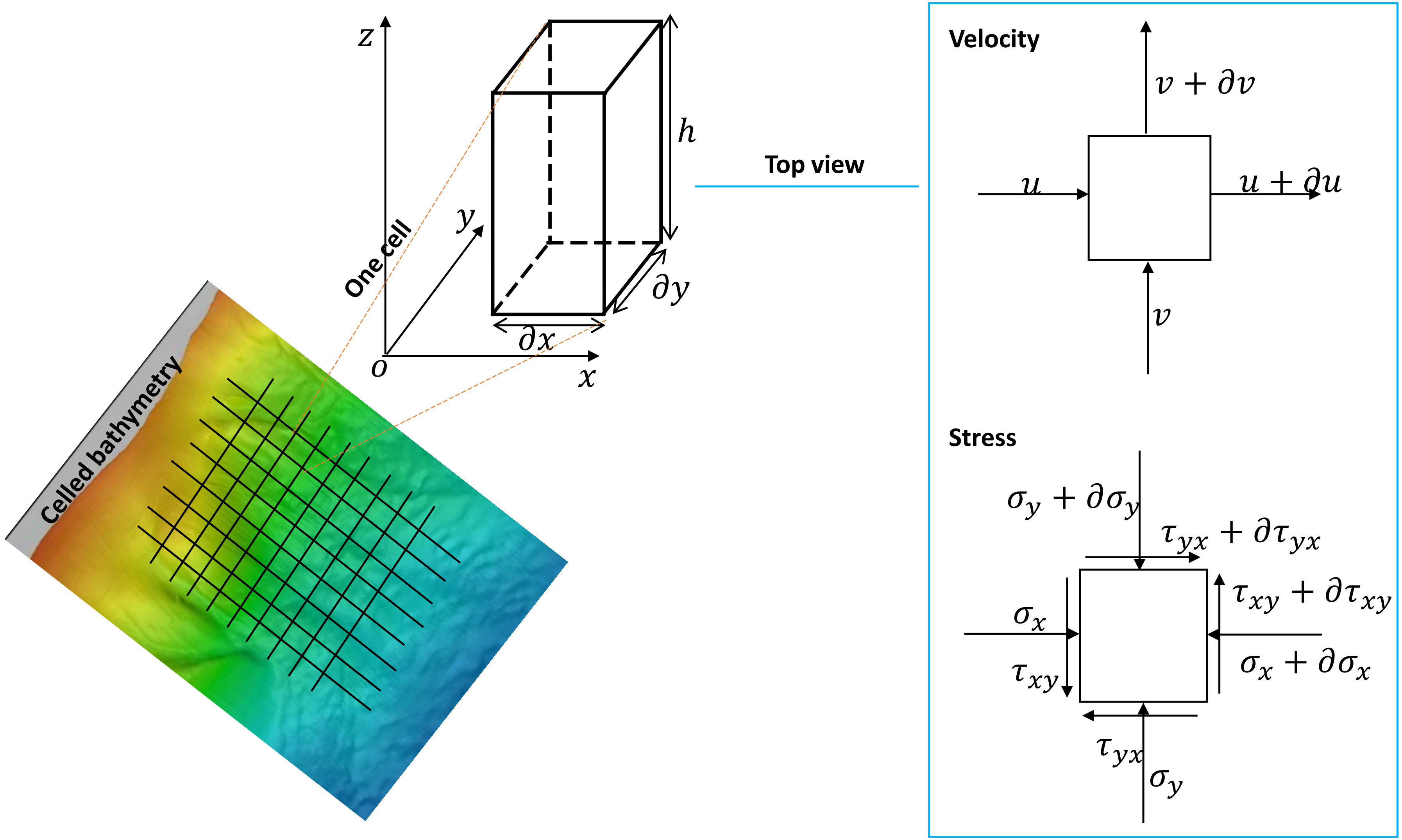

Figure 2 Discretisation and velocity and stress components of numerical model (bathymetry image shows the main scar of the Loch Eriboll Slide, after Carter et al. 2020)

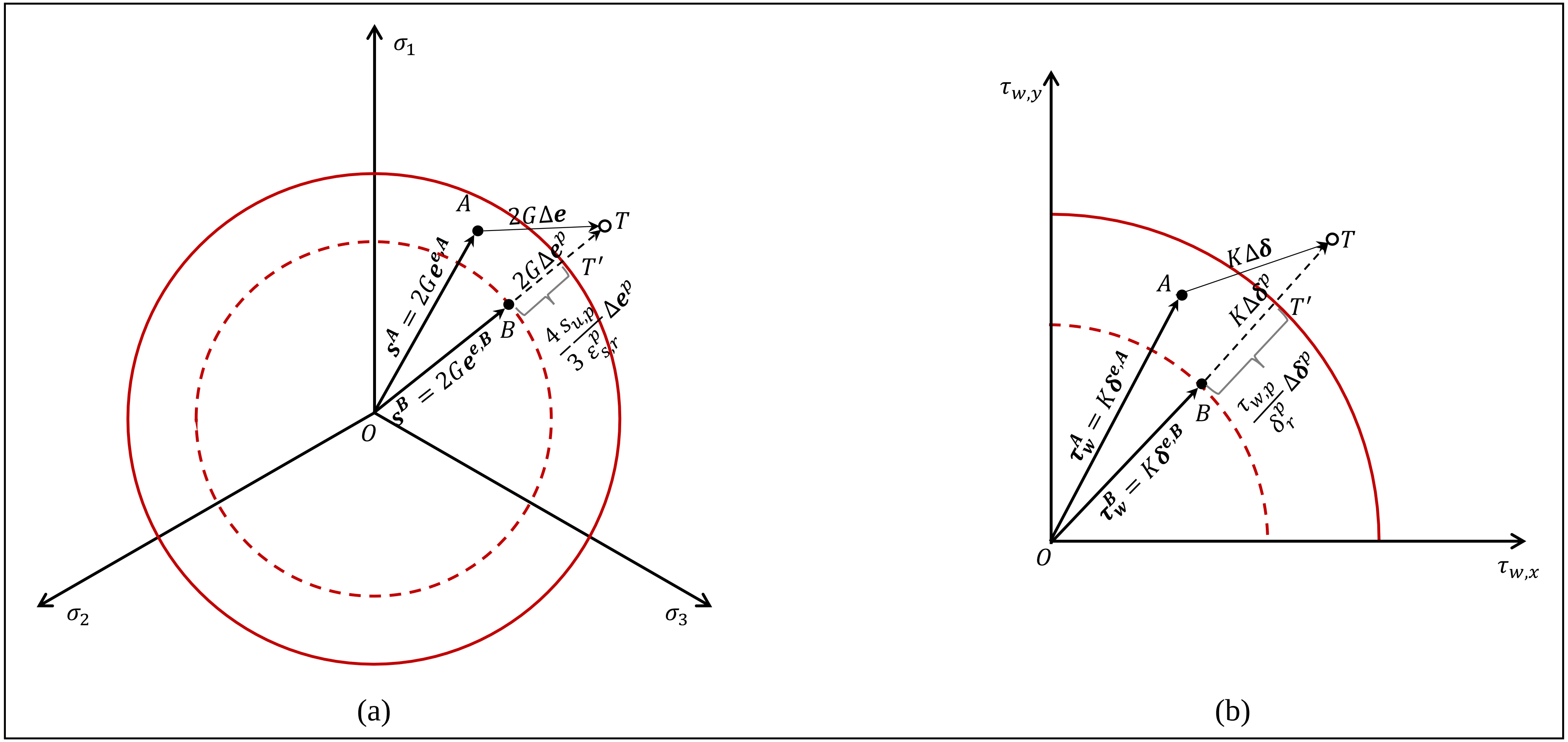

Figure 3 Constitutive models of soils in (a) sliding layer and (b) weak layer

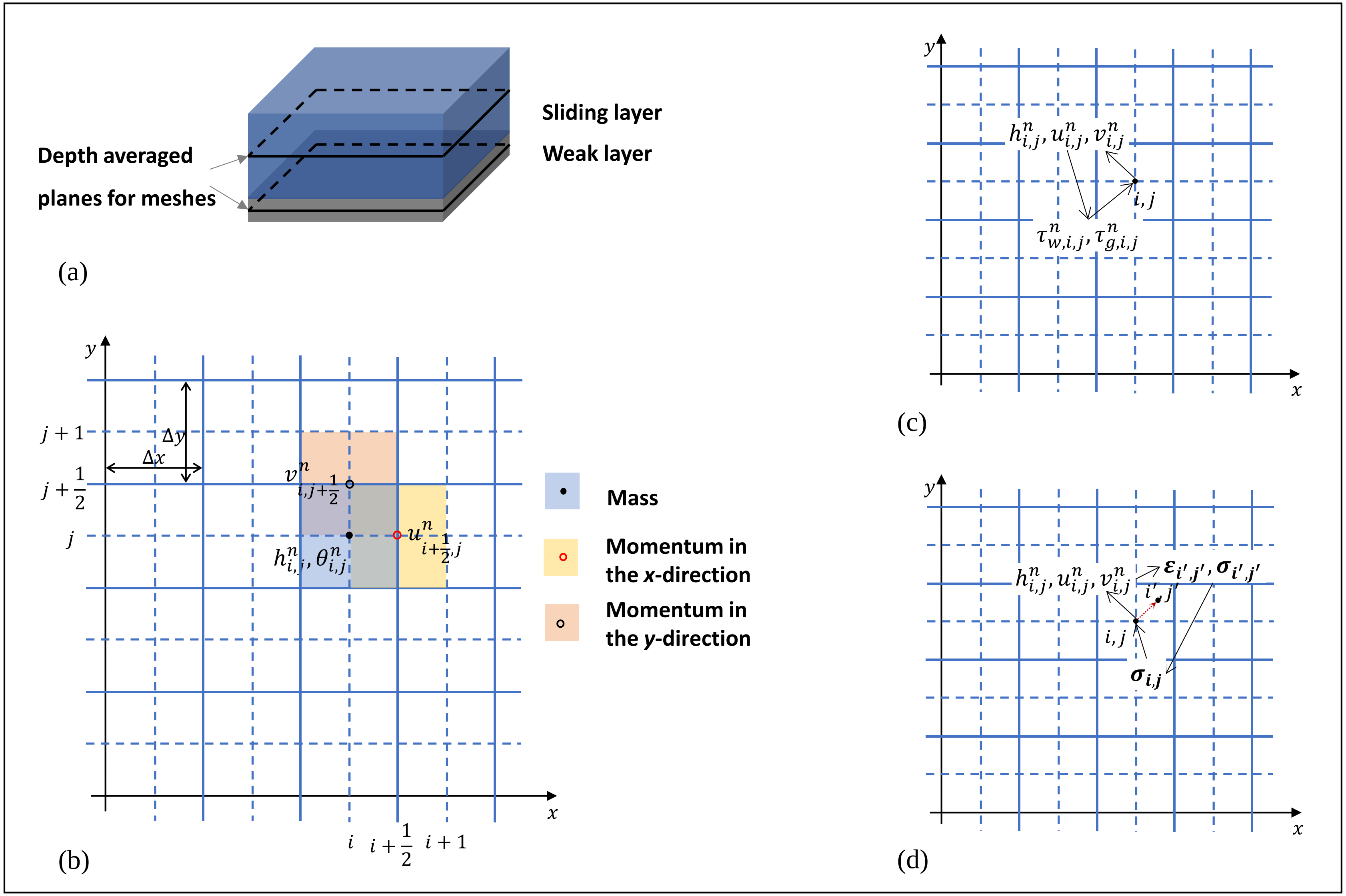

Figure 4 (a) Schematics of depth integrated model; (b) staggered mesh scheme; (c) update of properties for the fixed weak layer; and (d) update of properties for the movable sliding layer

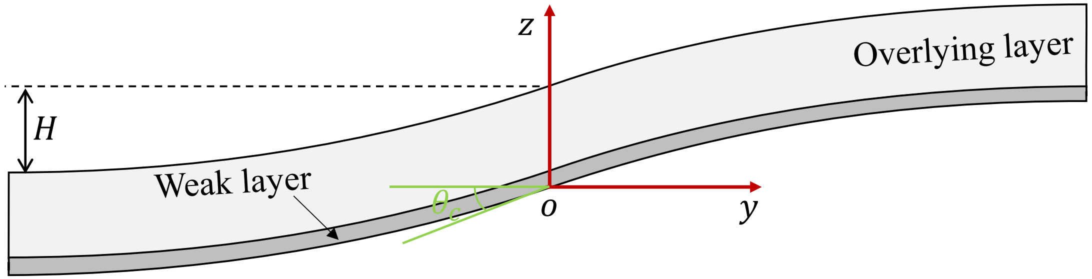

(a)

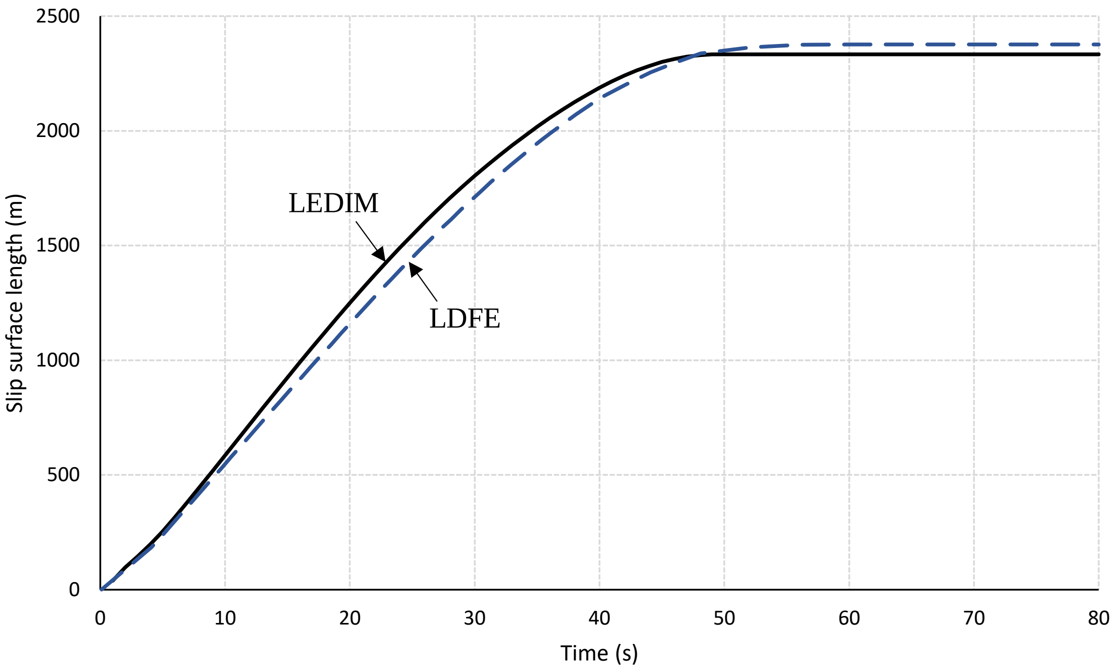

(b)

Figure 5 (a) Model used for verification case: 2D slope with 1D slip surface growth; (b) comparison of slip surface length obtained by large deformation finite element (LDFE) modelling and by the proposed depth integrated numerical scheme

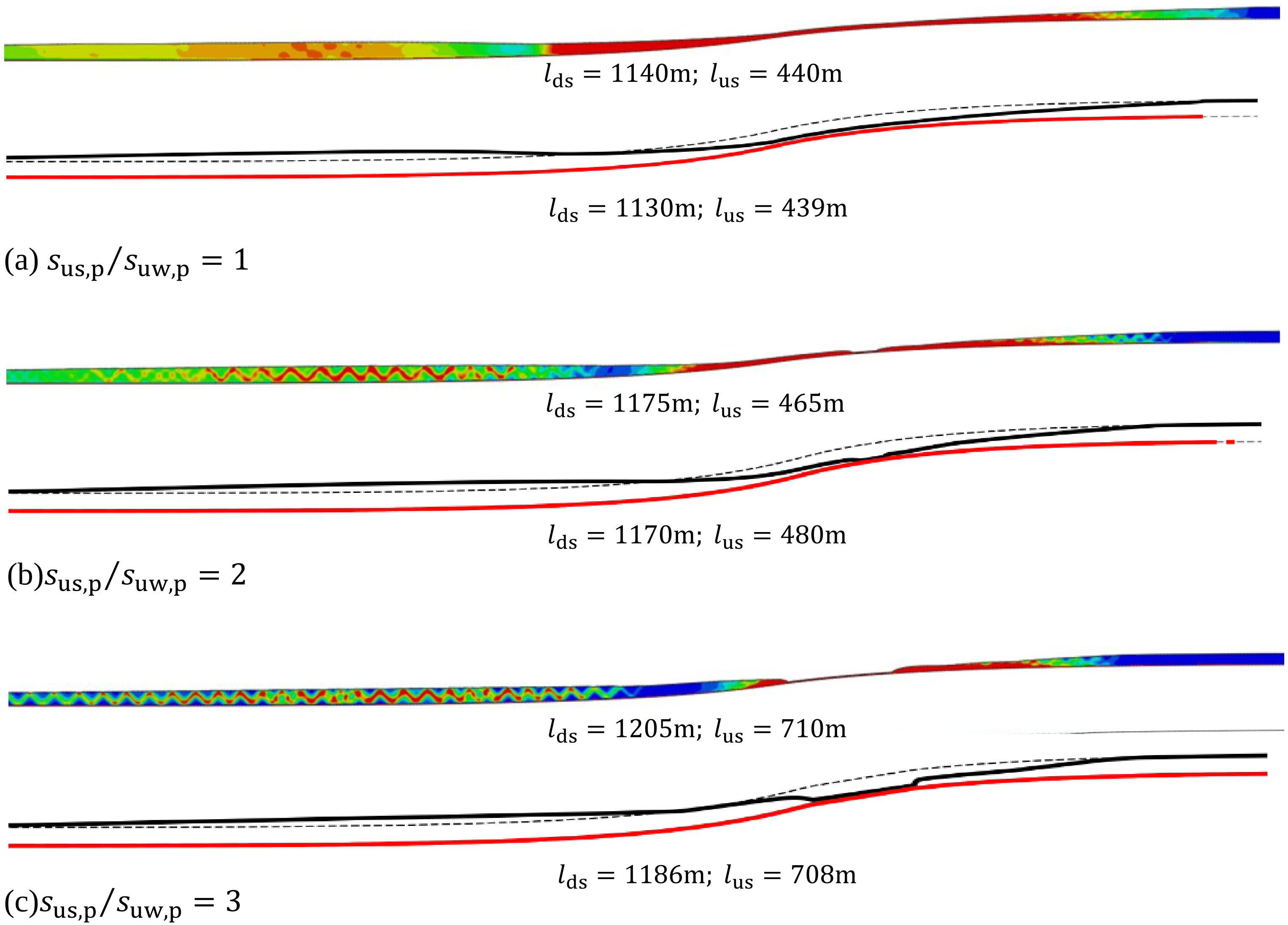

Figure 6 A comparison of two-dimensional post-failure configuration by large deformation finite element (LDFE) modelling and proposed depth integrated numerical scheme

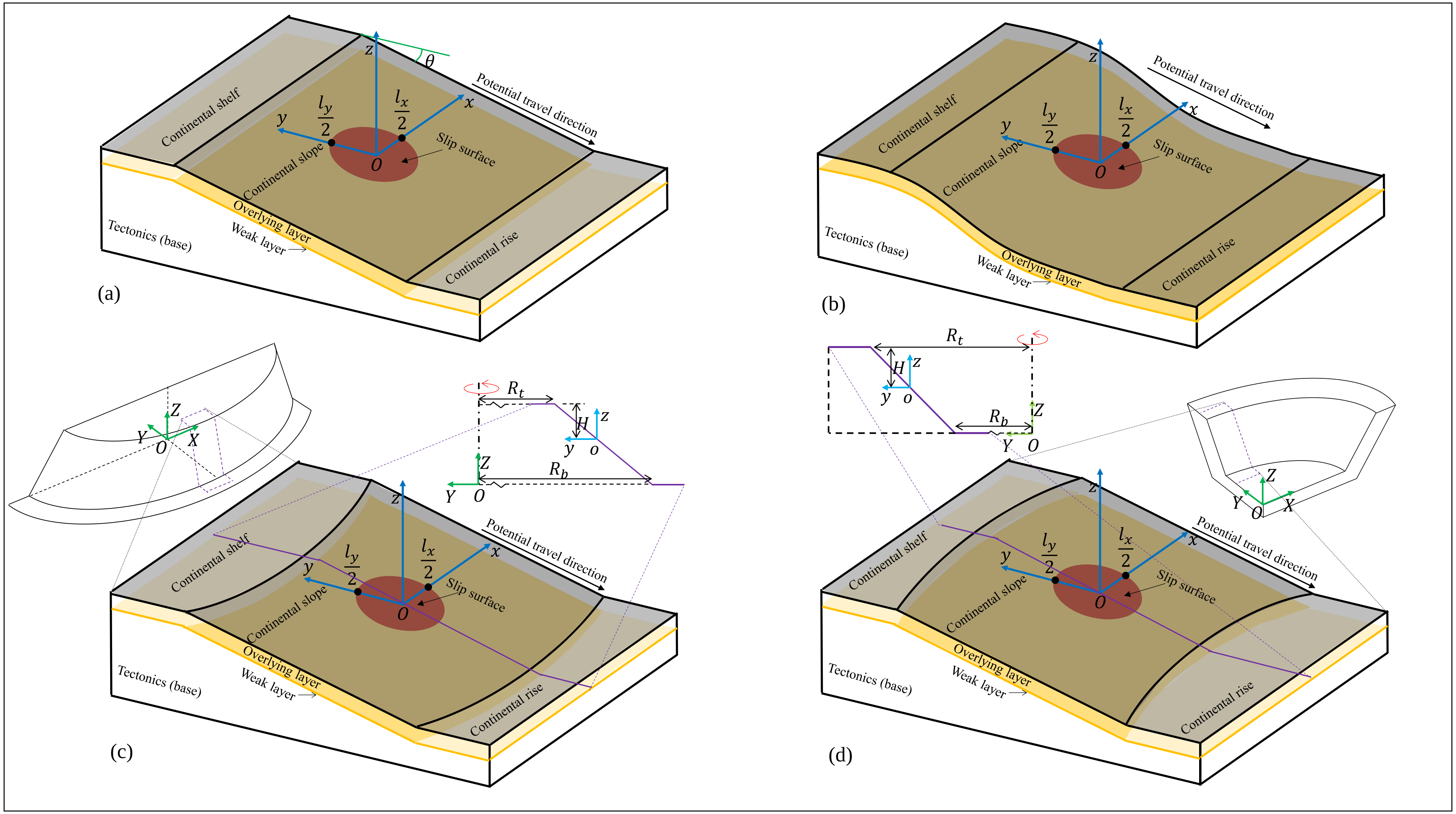

Figure 7 Conceptual 3D submarine slope models used in the study: (a) planar; (b) S-shape; (c) convex; and (d) concave

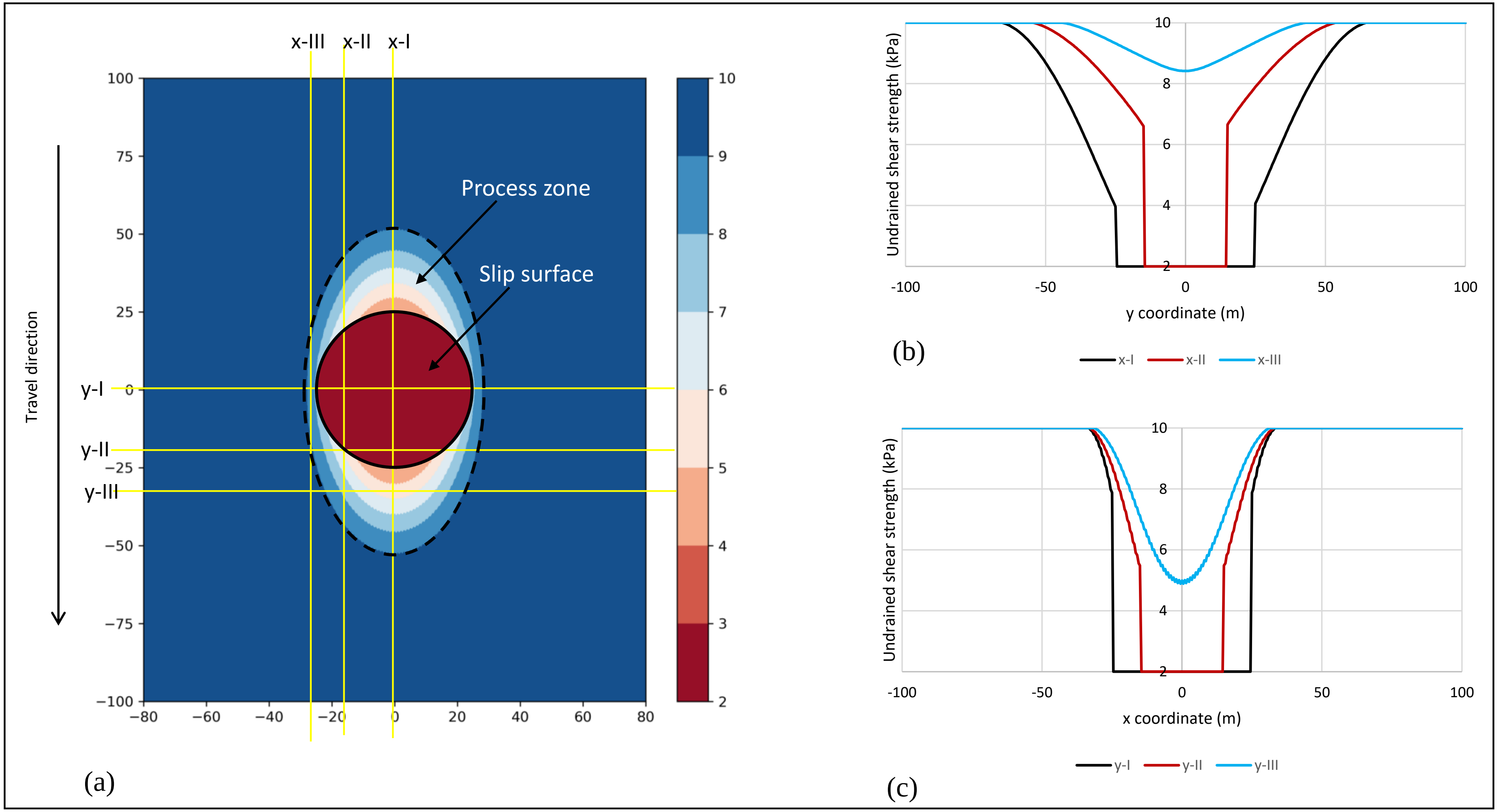

Figure 8 A typical case with stable growth of slip surface: (a) shear strength contour; (b) distributions of shear strength along cross sections parallel to *x-axis*; and (c) distributions of shear strength along cross sections parallel to y-axis

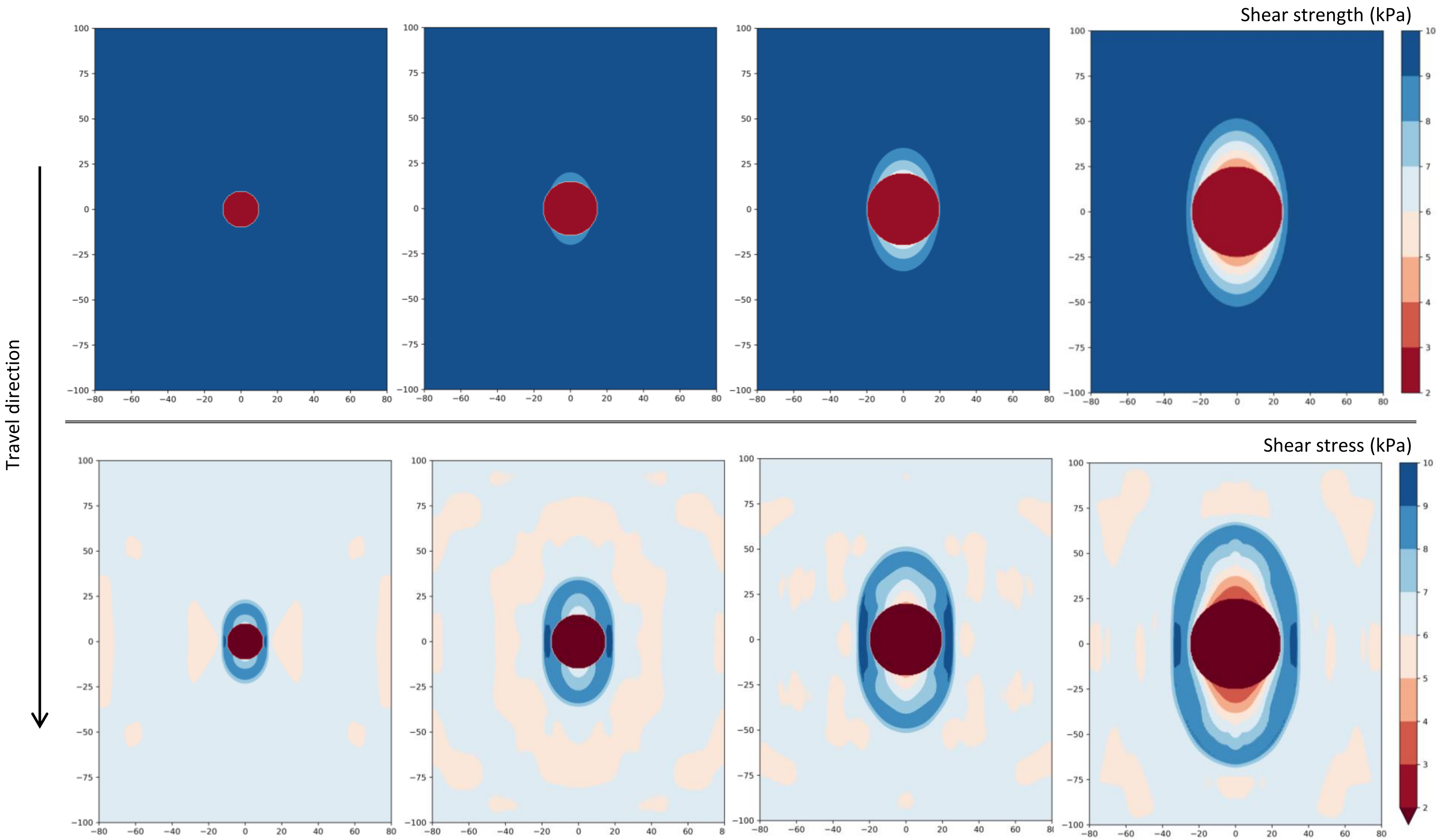

Figure 9 Evolution of shear strength (top row) and shear stress (bottom row) contours during stable growth of slip surface for a typical case

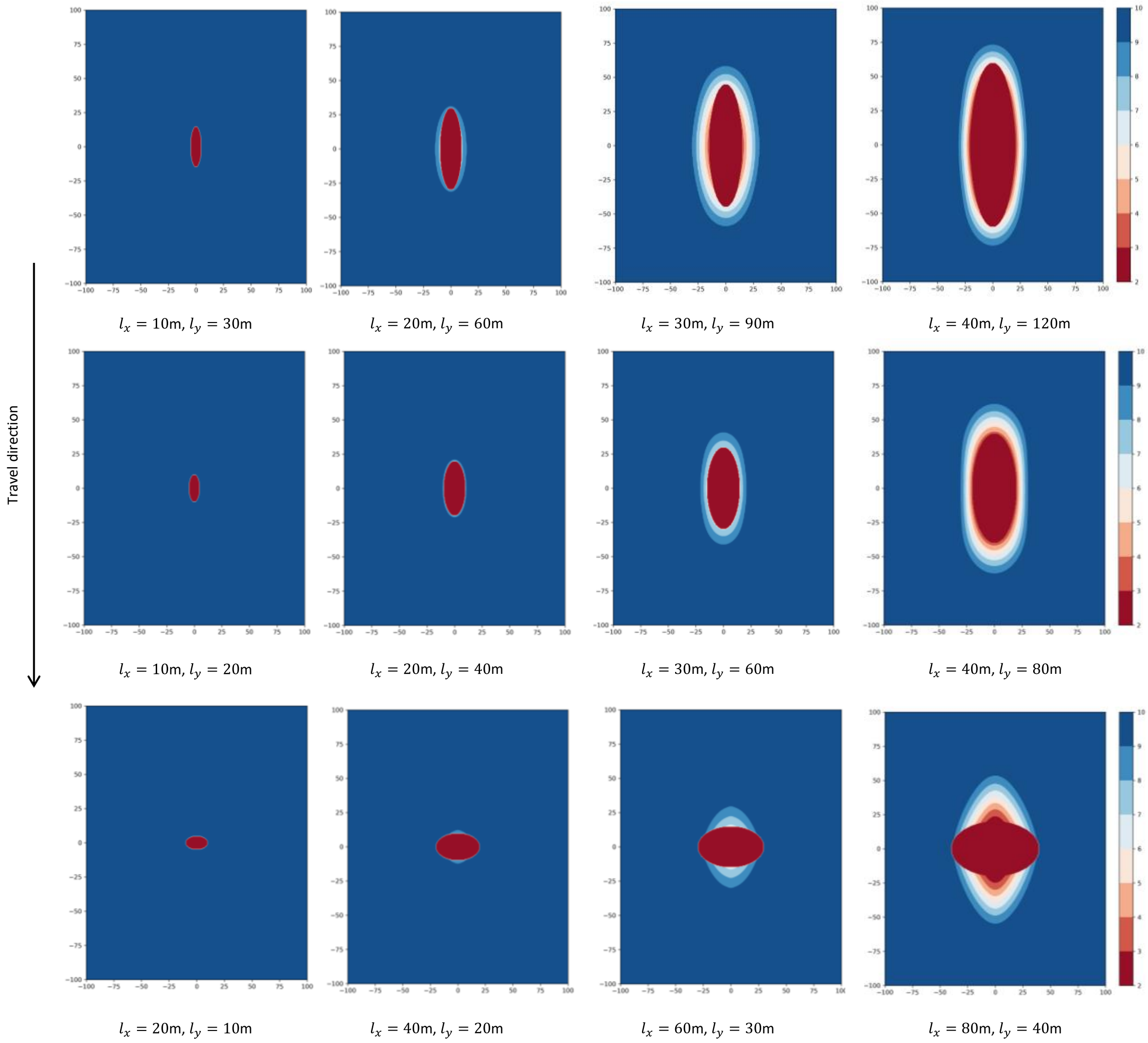

Figure 10 Stable growth of slip surface with different sizes and shapes of initiation zone

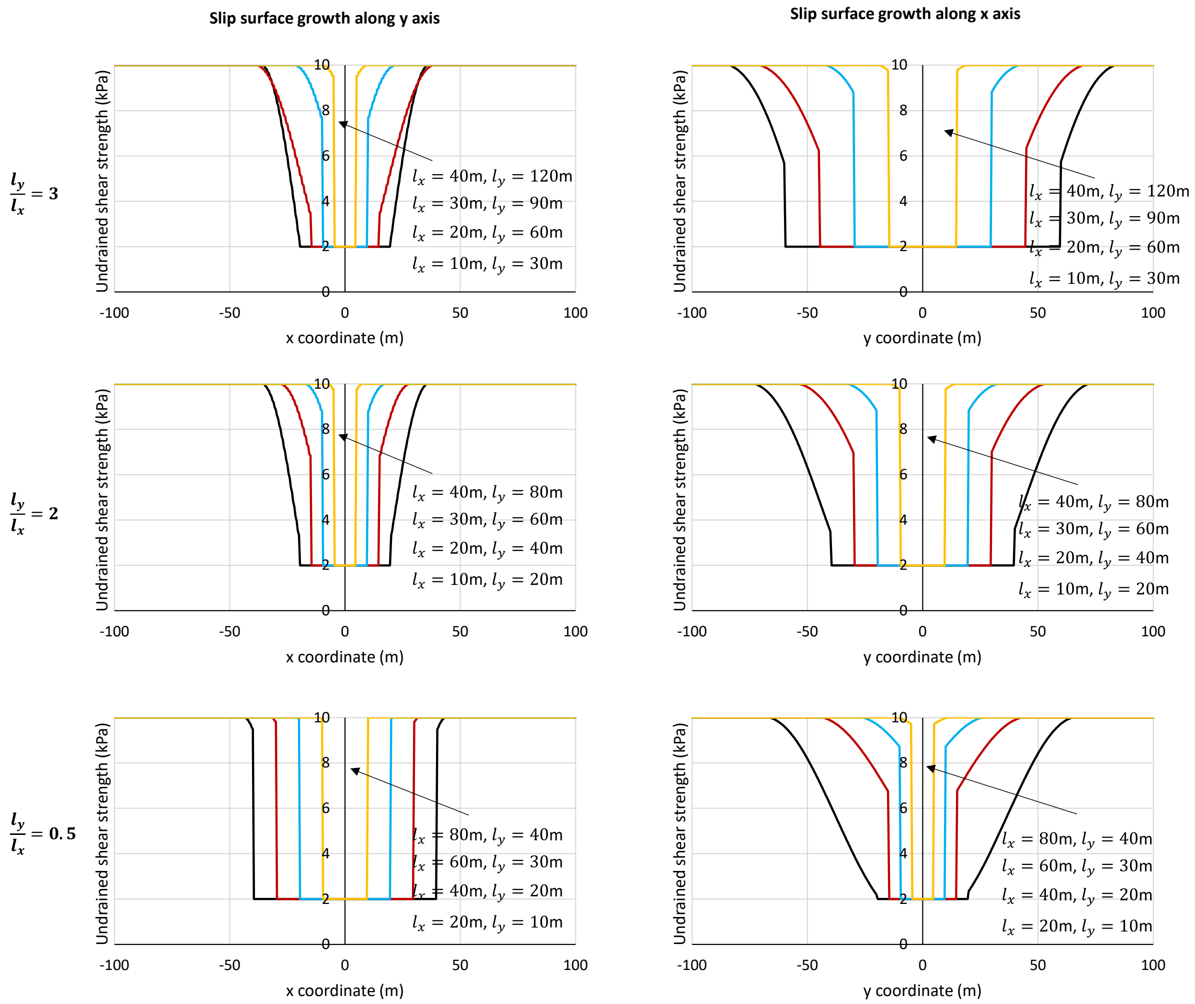

Figure 11 Distributions of shear strength along the *x*- and *y-axes during* stable growth of slip surface with different sizes and shapes

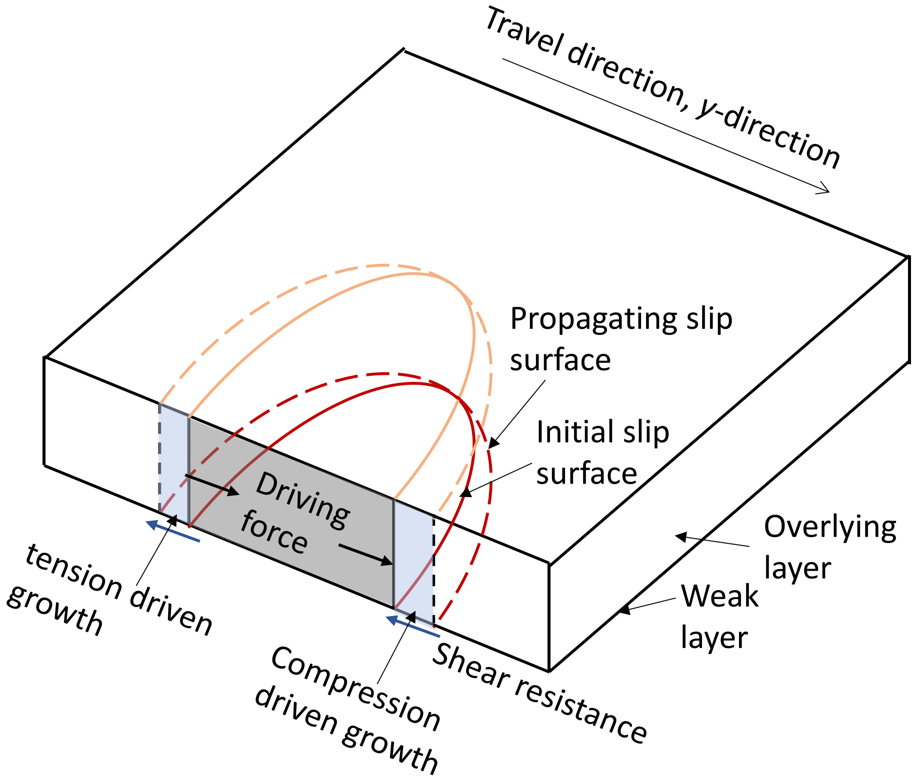
Travel direction, y-direction
Propagating slip surface
Initial slip surface
Driving force
Overlying layer
Weak layer
tension driven growth
Compression driven growth
Shear resistance

(a)

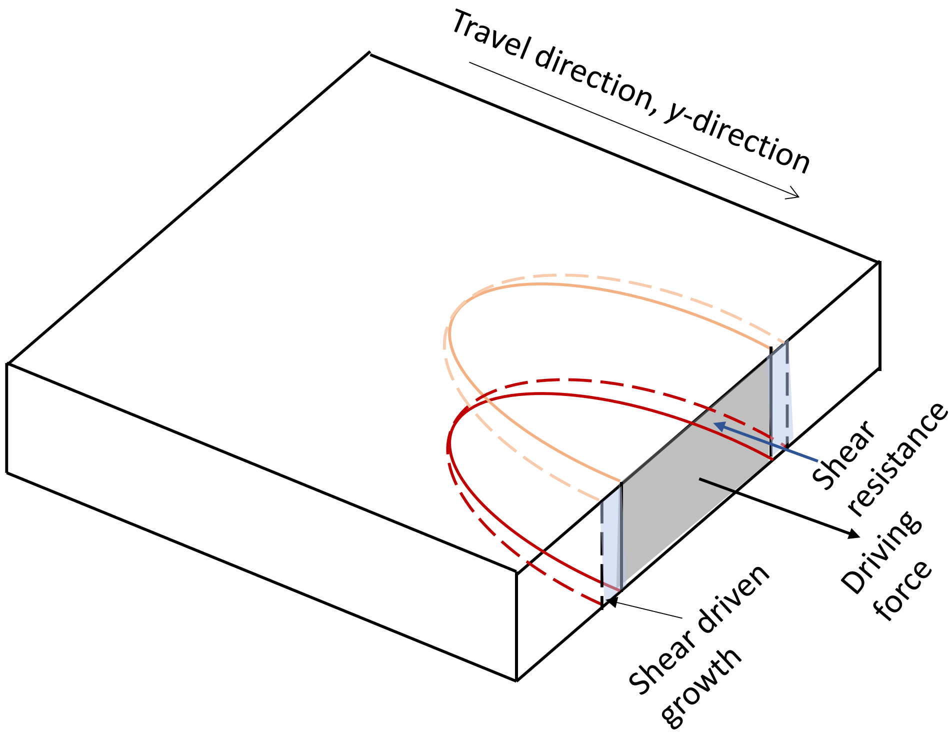
Travel direction, y-direction
Shear resistance
Driving force
Shear driven growth

(b)

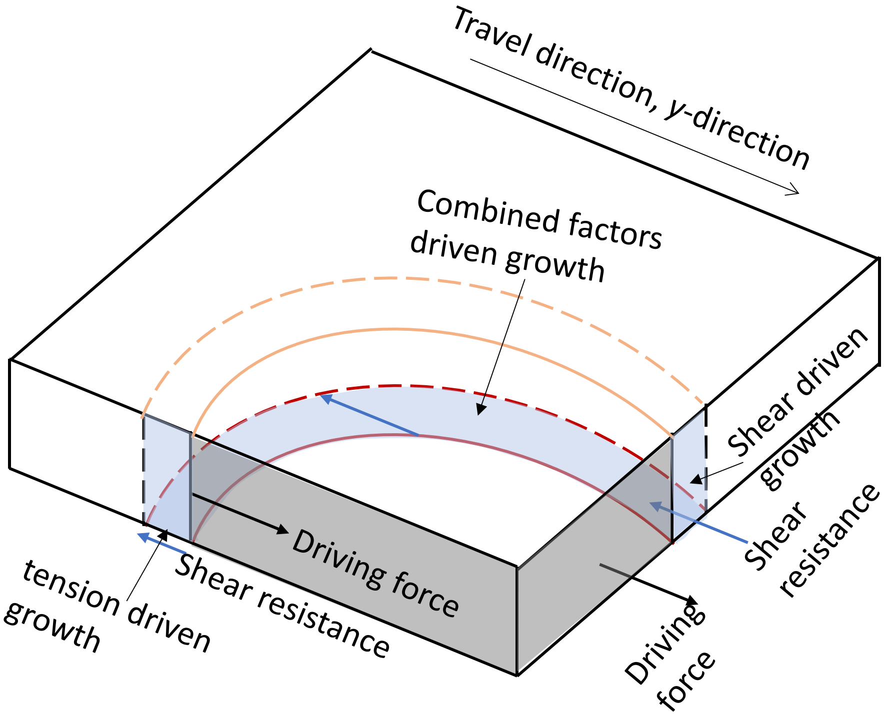

(c)

Figure 12 Three slip surface growth modes: (a) compression-extension mode; (b) shear mode; and (c) combined mode

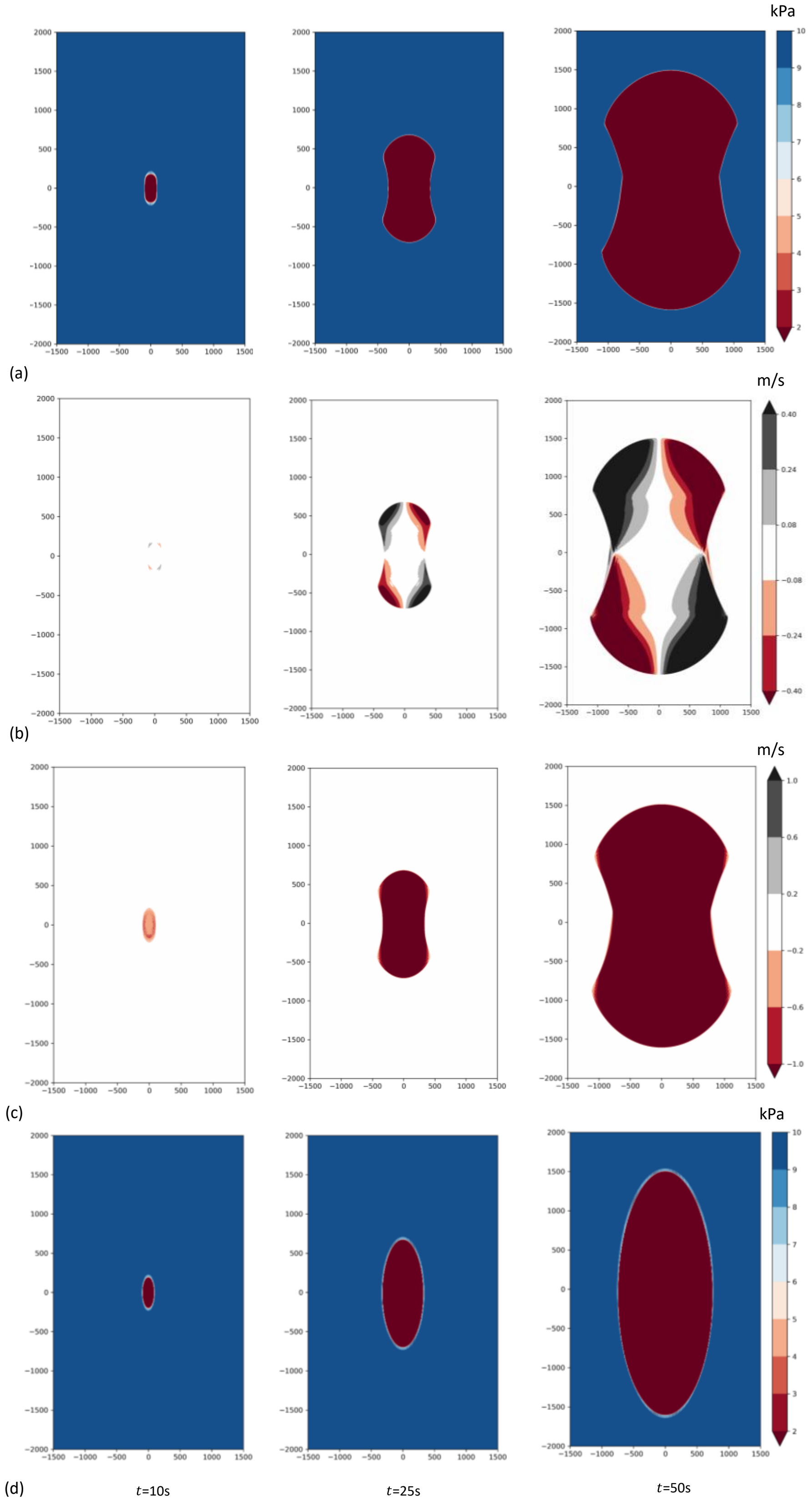

Figure 13 (a) Shear strength contours, (b) horizontal velocity contours and (c) vertical velocity contours for the case of free movement in x direction (perpendicular to the travel direction); and (d) shear strength contours for the case of restricted movement in x direction

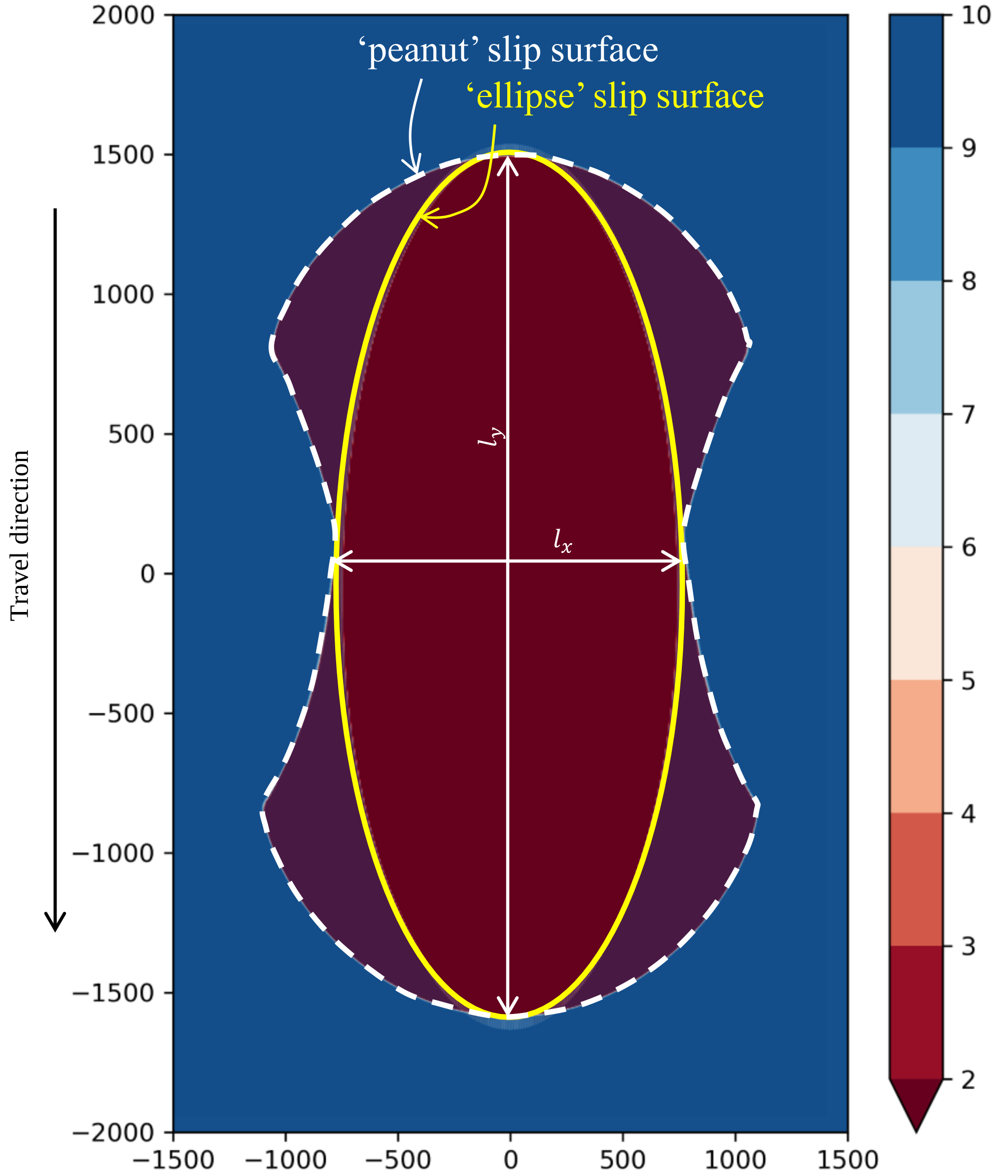

Figure 14 Two mechanisms for unstable growth of slip surface

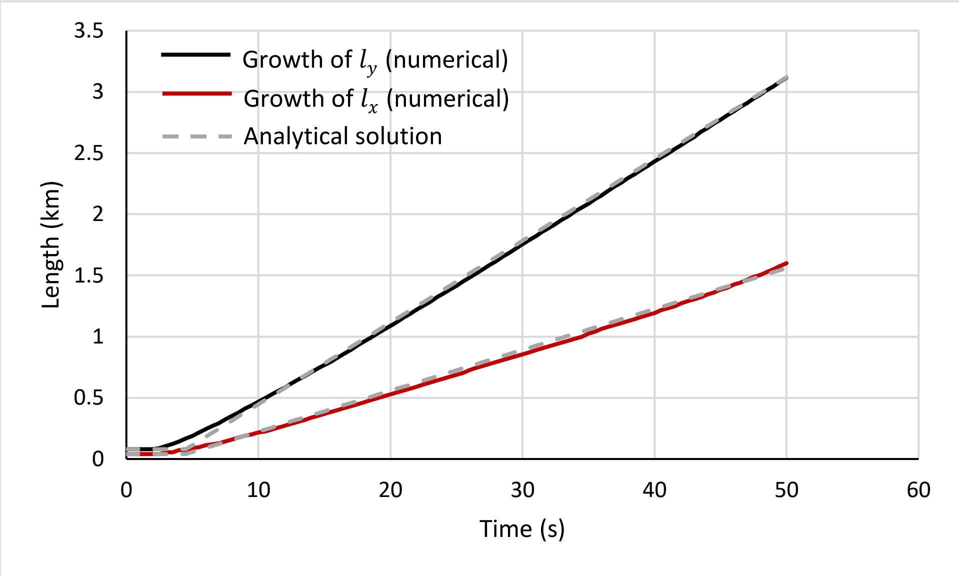

(a)

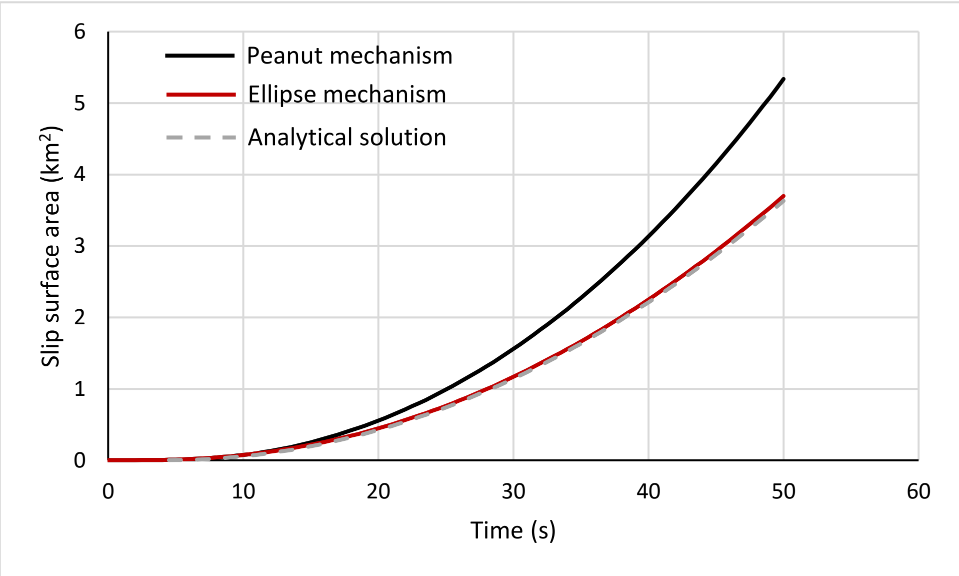

(b)

Figure 15 Speed of slip surface growth in terms of (a) major and minor axis lengths and (b) area of slip surface

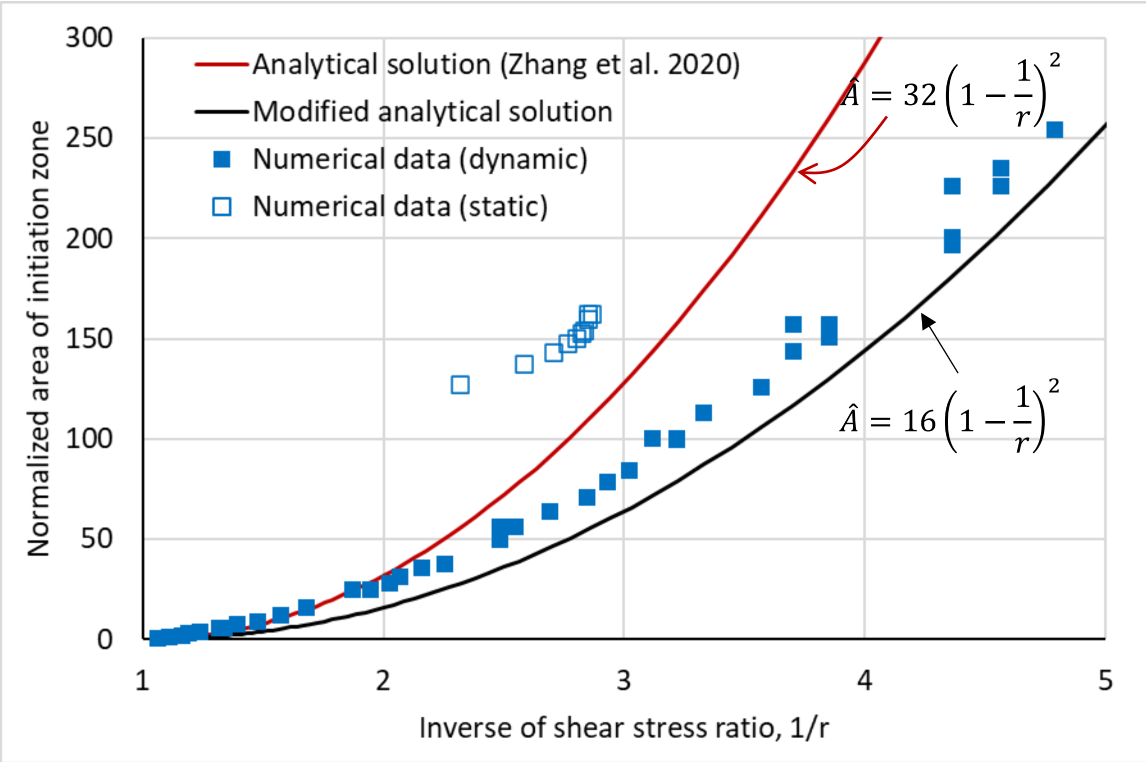

(a)

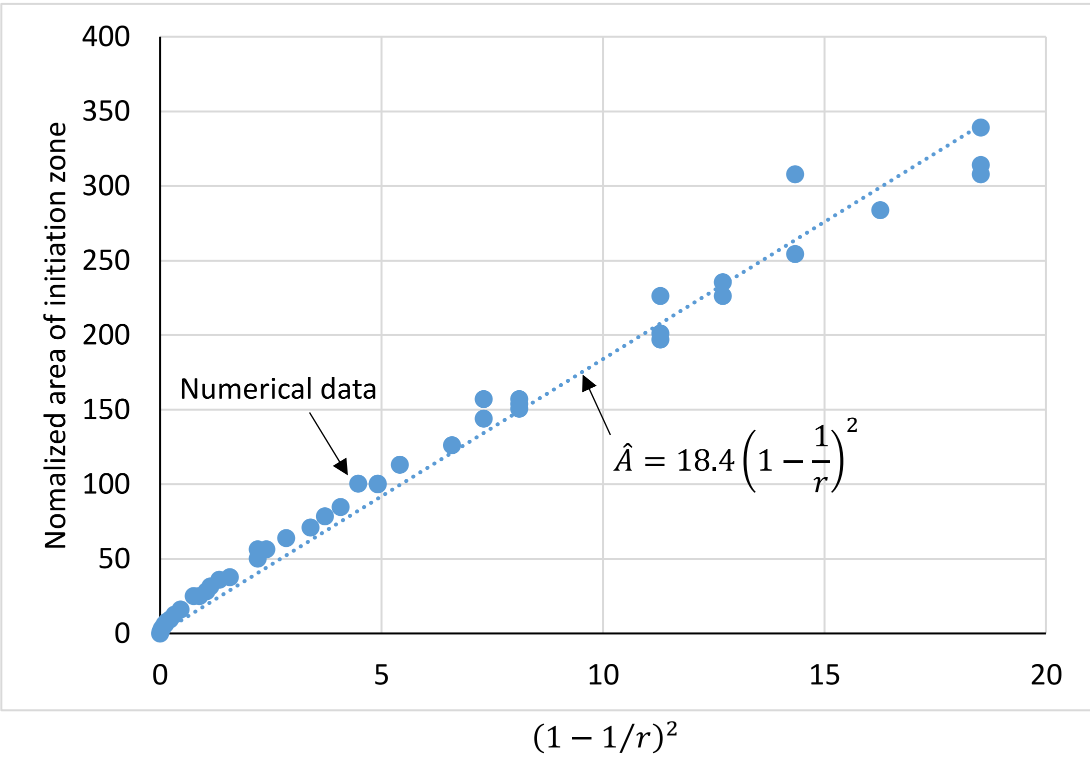

(b)

Figure 16 (a) Critical area of slip surface for unstable growth by numerical and analytical analyses; and (b) best fitting of numerical data

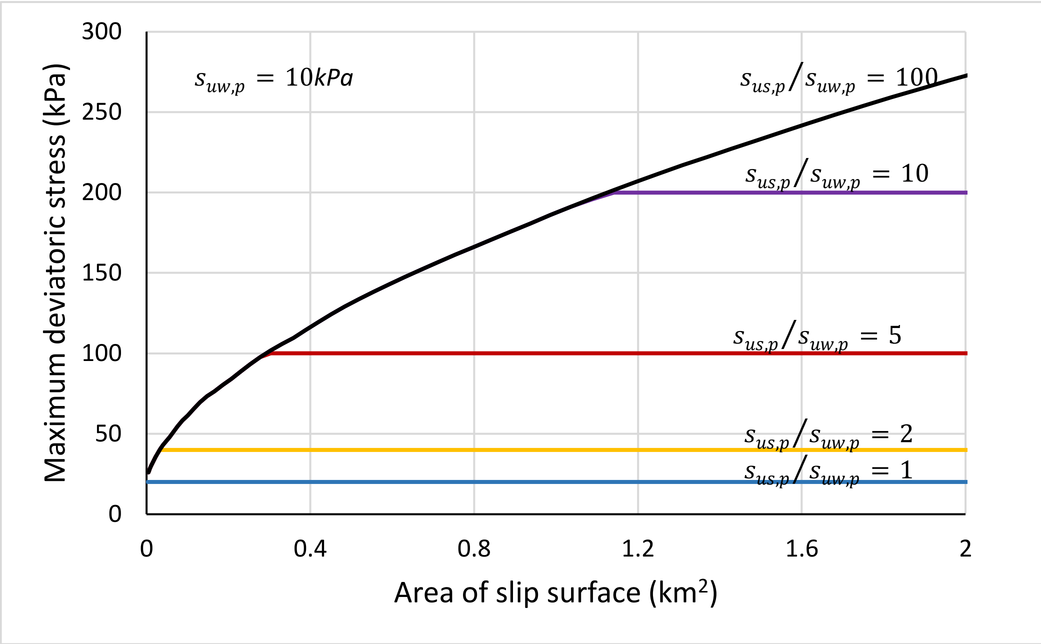

Figure 17 Maximum deviatoric stress in the sliding layer during unstable growth of slip surface

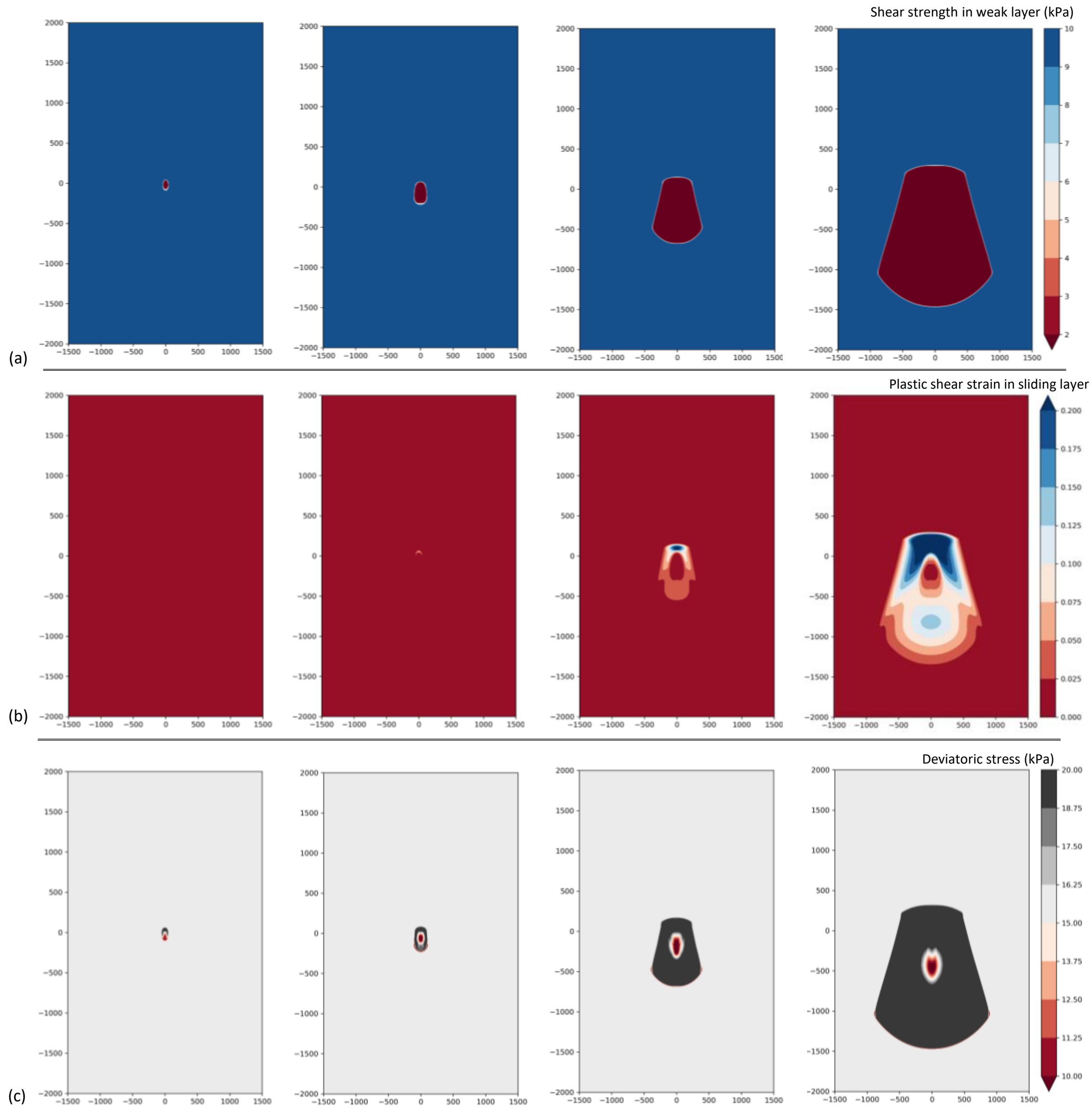

t=5s *t*=10s *t*=25s *t*=50s

Figure 18 Contours of shear strength in weak layer and plastic shear strain in sliding layer for the case with $s_{\mathrm{us,p}}/s_{\mathrm{uw,p}} = 1$ and $K_0 = 0.5$

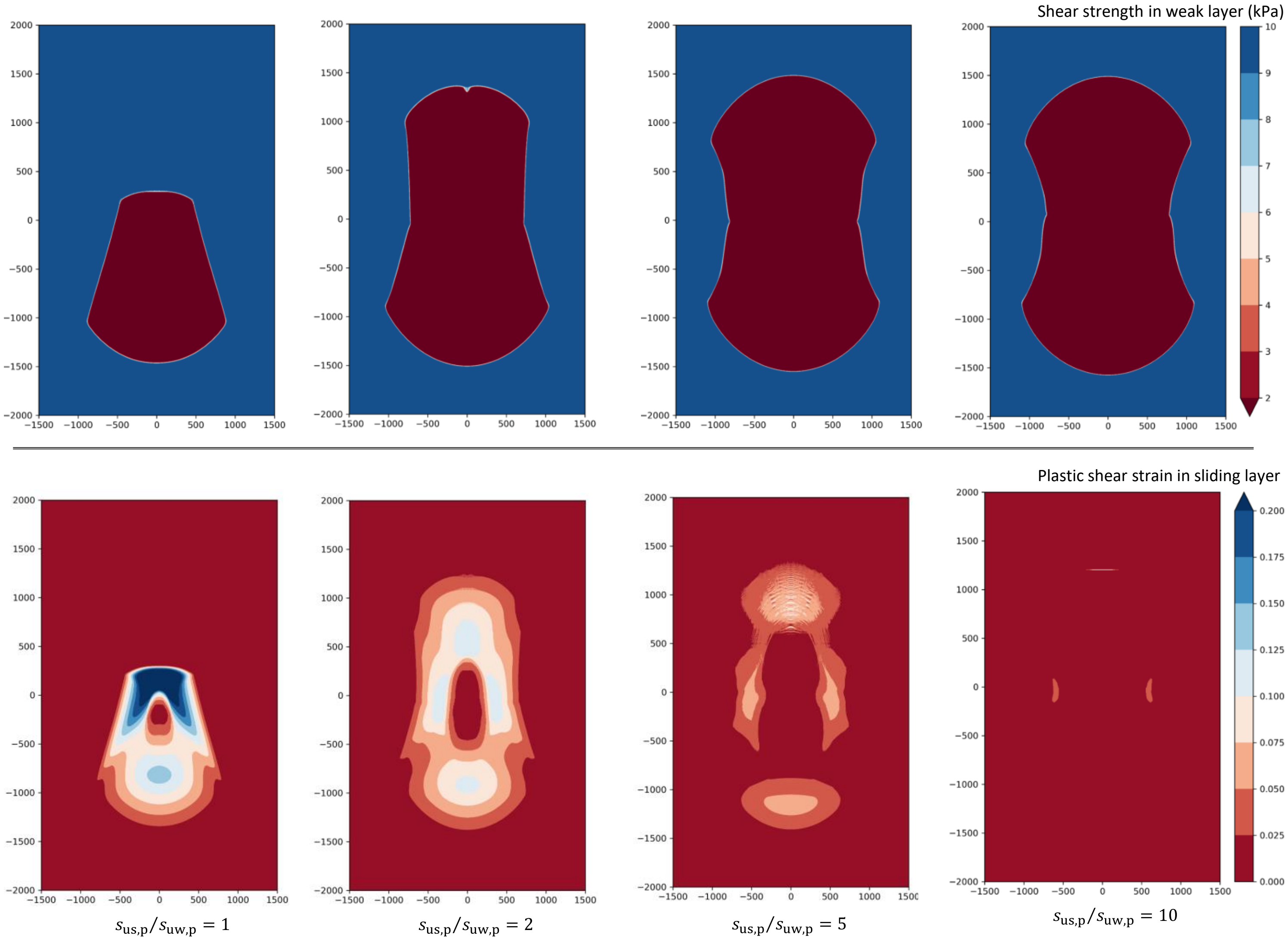

939

940 Figure 19 Contours of shear strength in weak layer and plastic shear strain in sliding layer for cases with different strength ratios $s_{us,p}/s_{uw,p}$

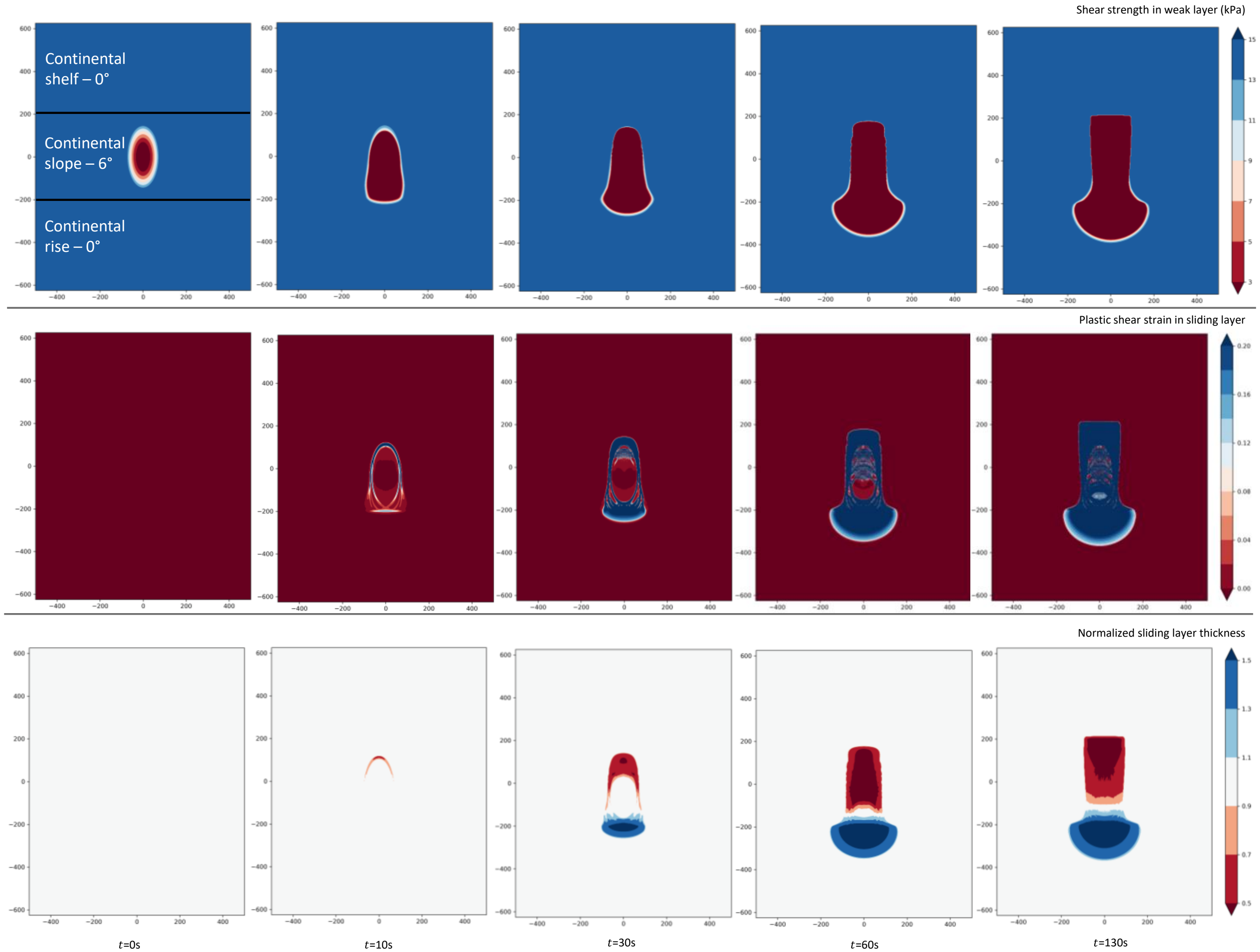
Shear strength in weak layer (kPa)
Continental shelf – 0°
Continental slope – 6°
Continental rise – 0°
Plastic shear strain in sliding layer
Normalized sliding layer thickness
t=0s
t=10s
t=30s
t=60s
t=130s

(a)

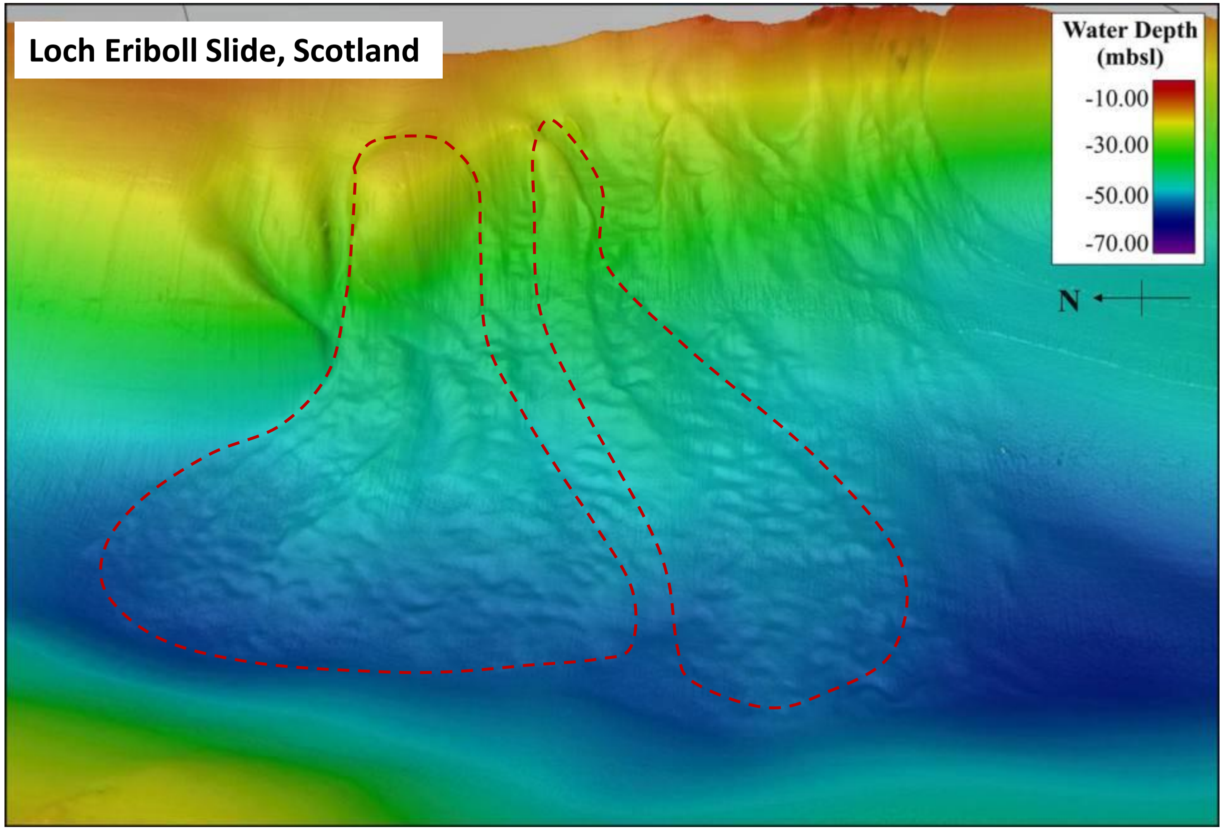

(b)

Figure 20 (a) Post-failure evolution of submarine landslides in terms of contours of shear strength in weak layer, plastic shear strain in sliding layer and normalised sliding layer thickness; (b) similar submarine landslide morphology discovered in the Loch Eriboll Slide (Carter et al. 2020)

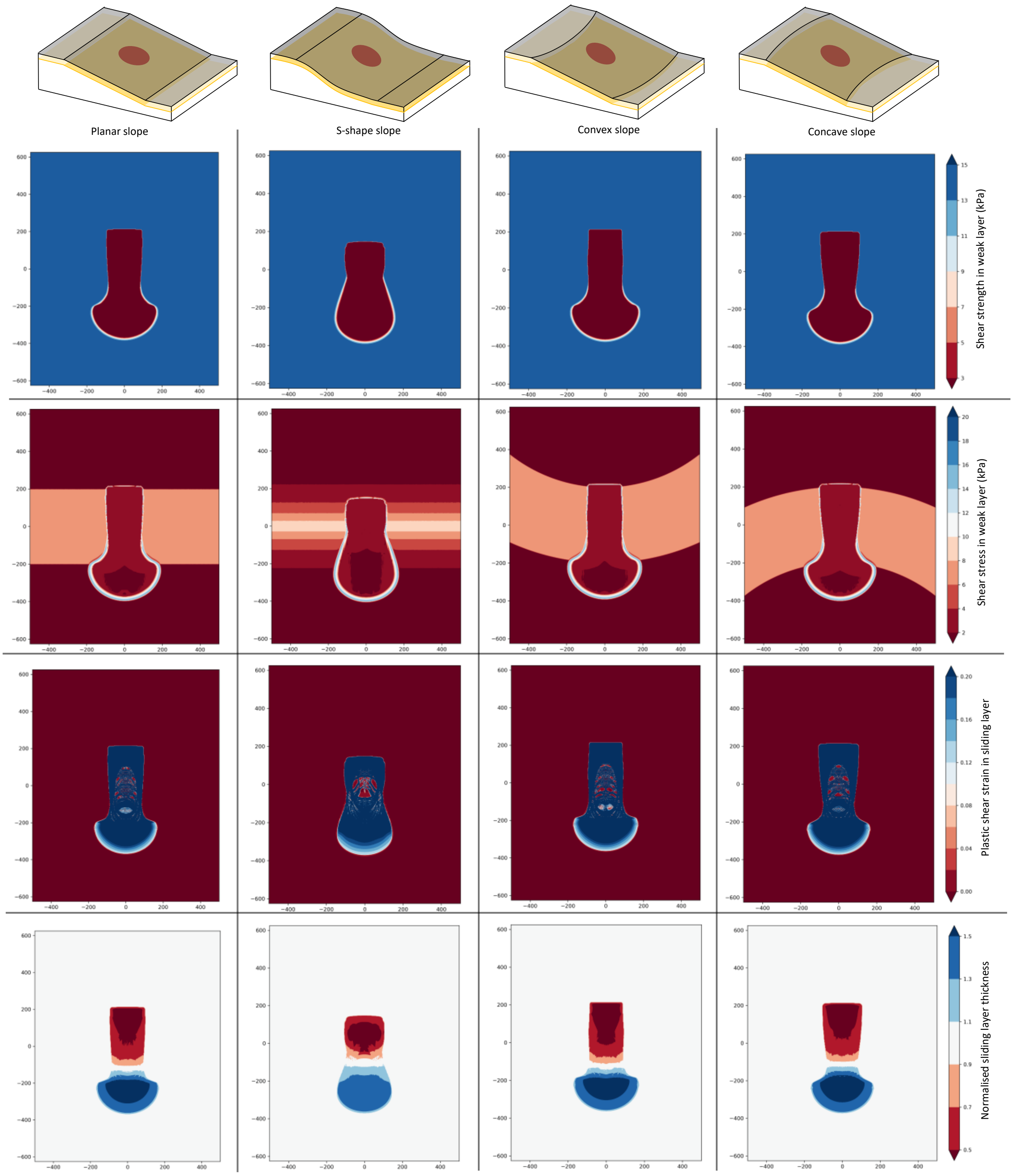

Figure 21 3D slope geometry effect on the ultimate slip surface growth and morphology of the mass transport deposit in translational landslides